Master's Thesis

Growth Study of Cuprate Thin Films by PLD

Yuichi Ota

February, 2010

Advisor
Professor Harold Y. Hwang

Department of Advanced Materials Science,
The University of Tokyo

Chance favours the prepared mind.

- Louis Pasteur

Preface

This thesis describes the work carried out for the Master's course in the Department of Advanced Materials Science, University of Tokyo. The central topic is to optimize the growth condition of cuprate thin films. In prospect for fundamental physics of high-T_c superconducting thin films and functional devices utilizing superconducting superlattice and ultra-thin films, it particularly focuses on $La_{2-x}Sr_xCuO_4$. Throughout this study, laser conditions and cooling procedure in PLD are mainly investigated. In addition, the installation of an ozone generator to the PLD system are successfully achieved to meet a requirement for enhancement of superconducting properties. Based on precise controlling of laser conditions, the way to obtain stoichiometric films with high-quality superconductivity is presented. The effect of ozone to the quality of thin films is also shown. These results lead to access the research field to study the physical properties in the artificial oxide interfaces utilizing cuprate thin films.

Yuichi Ota
February, 2010

Acknowledgments

Give a man a fish and you feed him for a day. Teach a man to fish and you feed him for a lifetime.

- An ancient proverb

First of all, I would like to express my greatest gratitude to Prof. Harold Y. Hwang for his support and encouragement. His fascinating, motivating, and stimulating words continuously drove me into research, taught me an enjoyment of science, and led me in the right direction. It is needless to say that this thesis would not have completed without his educational advice and continuous support.

I also would like to appreciate the members of this laboratory, Dr. Yasuyuki Hikita, Dr. Christopher Bell, Dr. Yanwu Xie, Ms. Makiko Tanaka, Mr. Yusuke Kozuka, Mr. Takeaki Yajima, Mr. Minu Kim, Mr. Motohide Kawamura, Mr. Satoshi Harashima, Mr. Yasuo Nakanishi, Mr. Hiroki Sato, Mr. Taro Wakamura, and Mr. Moyuru Kurita, as well as some of the former members, Dr. Kei S. Takahashi, Mr. Motoshi Nakayama, Mr. Takuya Higuchi, Mr. Mitsuru Nishikawa, Mr. Masayuki Hosoda, Mr. Kotaro Takeyasu, and Mr. Takeaki Hidaka and also collaborating visitors, Prof. Bog Gi Kim, Mr. Daeyoung Kwon, Mr. Bongju Kim, Mr. Youngsu Wu of Pusan National University, Prof. Jong-Hyun Song of Chungnum National University, Prof. Art Hebard and Ms. Guneeta Singh of the University of Florida, and Mr. James M. Rondinelli of the University of California at Santa Barbara. They all gave me good suggestions and opportunities to discuss scientific and daily topics. Especially, I am thankful that Dr. Yasuyuki Hikita and Mr. Yusuke Kozuka helped my daily work and for their discussions as my supervisors. I do not have the appropriate words to express my appreciation for their support.

Prof. Hidenori Takagi and Prof. Mikk Lippmaa allowed me to use their equipment, and I would like to show my appreciation for their experimental support. When setting up the ozone generator into the pulsed laser deposition system, I received much practical advice from Dr. Ichiro Tsukada in the Central Research Institute of Electric Power Industry. I am especially grateful to him for giving me an opportunity to visit his laboratory and for offering an explanation of ozone use. For technical support in fabricating the components of the ozone generator, I am also grateful to Mr. Saito. Without his professional skill of metal processing, the set-up would have never been achieved.

My deepest gratitude to my family and my friends cannot be fully described here. Such happy and comfortable days in the University totally stands on the financial and mental support of my family. My friends have given me many wonderful and fulfilling memories.

From the bottom of my heart, I am proud of the three years I spent in the Hwang laboratory. Through the days full of ups and downs, I had many precious experiences which will definitely benefit me in the future. Finally, I would like to show my gratitude for all that I have seen, heard, and felt.

Contents

Chapter 1

Introduction

Oxide interfaces have recently been attracting a great deal of interest. In particular, transition metal oxide heterostructures are one of the central research fields since they exhibit various exciting physical properties such as high-T_c superconductivity and colossal magnetoresistance [1, 2]. As symbolized by the phrase Herbert Kroemer used in his Nobel lecture, "*the interface is the device*" [3], heterostructures hold enormous potential as innovative devices utilizing exotic phenomena. Not only that, the point to stress is that the heterostructure enables us to access unconventional properties appearing at interfaces which cannot be realized in the bulk phases. Recently, various attracting phenomena have been observed in artificially designed oxide interfaces including the charge discontinuity between oxide layers, such as $LaTiO_3/SrTiO_3$ [4], $LaAlO_3/SrTiO_3$ [5], and $La_{0.7}Sr_{0.3}MnO_3$/Nb-doped $SrTiO_3$ [6]. In addition, superconductivity in the $SrCuO_2$-$BaCuO_2$ superlattice is worthy to note because both $SrCuO_2$ and $BaCuO_2$ are individually not superconducting. The thin-film research revealing *hidden* physical properties at oxide interfaces is expanding.

$La_{2-x}Sr_xCuO_4$ can be a promising material to show unconventional properties when accommodated in heterostructures. As a typical example, the superconducting transition temperature T_c is strongly dependent on the epitaxial strain and oxygen configuration inside the film [7]. The recorded maximum $T_c = 51.5$ K was observed in a $La_{1.85}Sr_{0.15}CuO_4$ thin film under compressive strain with extra oxygen incorporation, even though T_c peaks at around 40 K in the bulk [8]. In a bilayer system, interfacial superconductivity has been discovered [9]. A bilayer combining an insulating La_2CuO_4 layer and a normal metal $La_{1.55}Sr_{0.45}CuO_4$ layer grown on a $LaSrAlO_4$ substrate showed superconductivity, which implies charge transfer across the interface. This has given rise to increasing interest in the mechanism of the interface superconductivity [7]. Additionally, ultrathin films of $La_{2-x}Sr_xCuO_4$ offers the possibility to approach the thin limit of high-T_c superconductivity presented in a single CuO_2 plane. As shown in Fig. 1.1, this material processes the simplest crystal structure among the high-T_c superconductors. Related to the crystal structure, the $La_{2-x}Sr_xCuO_4/SrTiO_3$ interface is also a fascinating system since it can include a built-in polar discontinuity between stacking layers. Some kind of reconstruction can be expected [10]. Furthermore, what should be emphasized is that

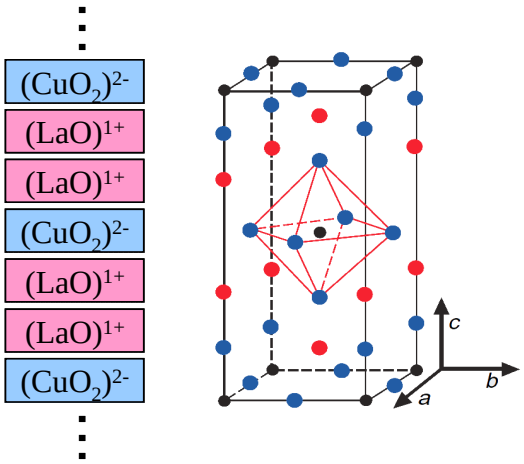

Figure 1.1: The crystal structures of La_2CuO_4 [12]. The sequence of the stacking layers along the c-axis is shown. Black, blue, and red circles indicate Cu^{2+}, O^{2-}, and La^{3+} ions, respectively.

the strong oxidization by ozone enhances the superconducting properties in thin films. Not only does it make T_c exceed the bulk value, it leads $La_2CuO_{4+\delta}$ to superconducting phase [11]. Thus, $La_{2-x}Sr_xCuO_4$ thin films teem with tremendous potential.

Pulsed laser deposition (PLD) is a suitable method for fabricating such thin films because it is a relatively simple and flexible technique for the deposition of high-quality films from multi-component targets. When we take on the challenge to explore the physical properties of artificial structures, this is a big advantage. It is, however, well known that precise control of the growth parameters is required. As suggested in the growth of titanates and manganites [13, 14], the optimization of the laser conditions is particularly important in addition to the control of the temperature and pressure. According to these results, the laser conditions significantly affect the cation ratio, which is a determinant factor of the physical properties. In other words, the optimization of the laser conditions is a crucial step to conduct research in the field of artificial structures utilizing $La_{2-x}Sr_xCuO_4$.

In this Thesis, we provide the basis to fabricate high-quality $La_{2-x}Sr_xCuO_4$ thin films especially focusing on the laser conditions and the oxidization process. We were able to optimize the laser condition and found a clear correlation between the laser density and the resistivity distribution. Additionally, we successfully introduced an ozone generator into the PLD system, resulting in the enhancement of film quality and superconducting properties. The outline of this Thesis is the following. In Chapter 2, the fabrication and characterization techniques are described in detail. In Chapter 3, the properties of ozone and the set up of the ozone generator are described. In Chapter 4, the crucial T_c determinants in $La_{2-x}Sr_xCuO_4$ system are summarized. In Chapter 5 and 6, the results and findings throughout this study are presented and discussed. In Chapter 7, the overall conclusion is presented.

Chapter 2

Fabrication and characterization techniques

2.1 Sample fabrication

2.1.1 Pulsed laser deposition system

As a method to fabricate thin films, pulsed laser deposition (PLD) has been adopted throughout this study. A schematic design of the system is illustrated in Fig. 2.1 (a).

Our system is composed of two vacuum chambers, the load lock chamber (L/L) and the main chamber. The L/L can be vented to atmospheric pressure, but the main chamber is not, in normal operation. This is because of the requirement to maintain a high vacuum and to eliminate impurity gases inside the main chamber. The sample is, consequently, introduced into the main chamber from the L/L, after loading into the L/L from outside. Sample fabrication is carried out inside the main chamber under precise temperature and pressure control.

The sample temperature is increased by a lamp heater, which is cooled by water flow (not shown in the figure). The maximum temperature is about 1000 °C. The temperature can be controlled by a proportional-integral-derivative (PID) system continuously and smoothly. The detailed set up of the PID system is described in Appendix A. As for the gases during growth, oxygen and ozone are introduced to main chamber. The pressure inside the chamber has a significant effect on the film growth so that the gas insertion and exhaust systems are both important. The nozzles of oxygen and ozone are separately installed. Their partial pressures can be modified independently. Each gas is introduced through a variable leak valve (VLV) (Varian, Inc.) whose minimum flow rate is 10^{-10} Torr·l/sec corresponding to a vacuum range of $\sim 10^{-11}$ Torr. For the gas exhaust system, one rotary pump (RP) and three turbo molecular pumps (TMPs) pump the main chamber. The base pressure in the main chamber is lower than 1×10^{-8} Torr. In addition to the above systems, a shutter and a valve are set in order to control the gas flow inside the chamber. When controlling the pressure, one needs to coordinate the gas insertion system, the gas exhaust system, the shutter and the valve appropriately (Appendix A).

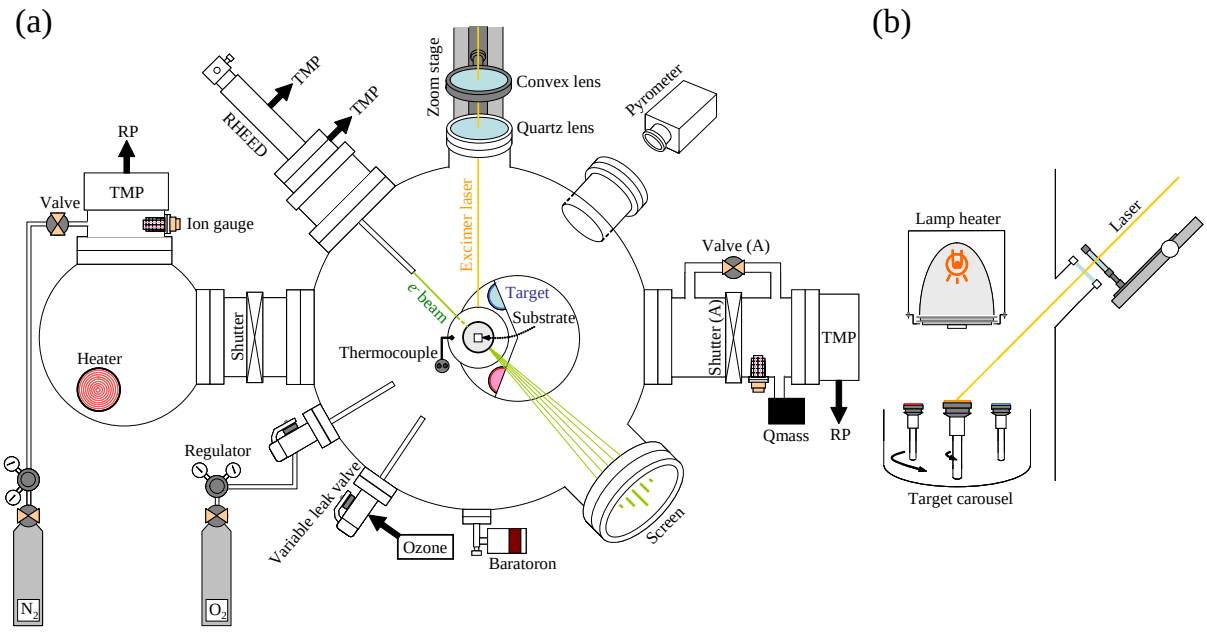

Figure 2.1: (a) Schematic overview of the PLD system, and (b) the ablation process.

After adjusting the temperature and pressure appropriately for the growth conditions of each material, the sample fabrication is carried out. PLD is, as the name suggests, a method to deposit laser-ablated materials on the substrate. As the source of energy for evaporation, a pulsed KrF excimer laser is used with a wavelength of 248 nm and a pulse duration time of ∼25 ns. As shown in Fig. 2.1 (a), the laser beam is introduced into the chamber through a convex lens and a quartz plate. The laser-ablated target material immediately evaporates and quickly turns into a plasma. Each element of the material travels to the substrate, and is influenced by the atmosphere and the laser conditions (discussed later). Just at the moment the species reach the substrate, they cool rapidly after diffusing on the surface of the substrate and arriving at an energetically stable position. This process can be directly monitored by the reflection high-energy electron diffraction (RHEED) system. The electron beam of the RHEED irradiates the surface of the substrate at a small incident angle. After scattering at the surface, the diffraction pattern appears on the phosphor screen. Since the pattern and intensity indicate the periodicity of the surface, one can monitor the growth mode *in situ* through the changing intensity of the diffraction spot.

Compared to other methods such as molecular beam epitaxy (MBE), PLD has great advantages for the fabrication of oxide thin films in the following aspects. Firstly, PLD is suitable to grow multi-component materials. This characteristic is important because the target oxide materials used in this study have a complex composition. They often contain three or four elements. In addition, the cation ratio decides their physical properties in many cases, in other words, the deviation of the cation ratio means the appearance of unexpected physical properties. The laser ablation process in PLD, however, can directly transfer the target composition to the substrate keeping its cation ratio under the

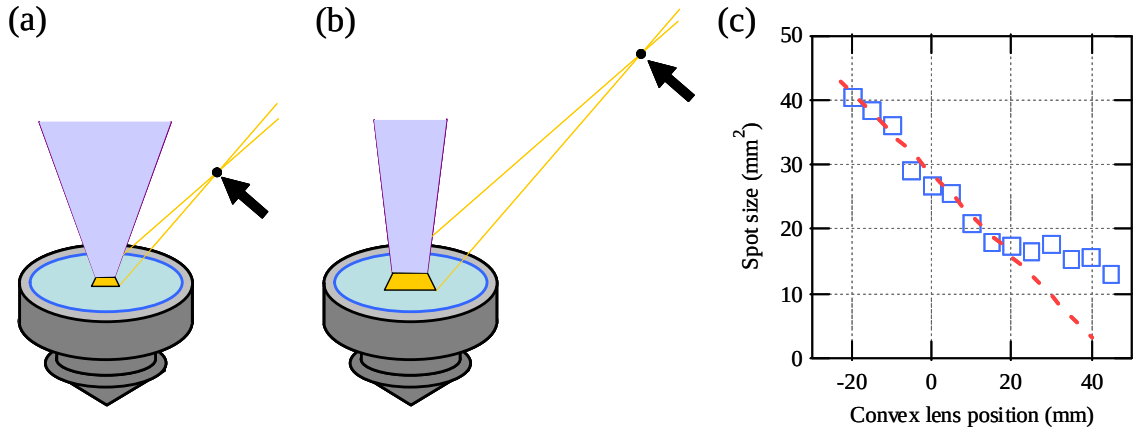

Figure 2.2: The schematic illustration of laser ablation and plume distribution at the surface of the target when the spot size is (a) small and (b) wide. The black arrows indicate the focal position. (c) The spot sizes are measured as the position of the convex lens is changed. The spot size is defined as the discolored area of a photo-sensitive paper ablated by the excimer laser. The dashed red line is fit in the range of convex lens position -20 from 20 mm.

optimized conditions of atmosphere and laser ablation. Thus, one can avoid fine-tuning the evaporation rates of each element, as required in MBE, so that one can control the physical properties of the film by design. Secondly, it is easier to make a superlattice structure *in-situ* in PLD. It is only necessary to prepare several targets in advance. Target exchange in PLD does not require breaking the main chamber vacuum unlike the case of MBE, which makes PLD a suitable method for making multi-component superstructures. Artificial structures never seen in nature could be one of the candidates which open new fields of physics. In addition to the above, it is important in PLD to provide sufficient energy to evaporate the target materials. Many oxides have high melting points, exceeding 1000 °C. The laser ablation process, however, has the energy to break the chemical bonds and form a plasma of each element. Consequently, almost all oxide materials are candidates to be targets.

2.1.2 Laser condition

It has been pointed out that one should optimize the laser condition for each target material as well as the temperature and pressure in order to achieve the stoichiometric transfer of the target material to the substrate. In particular the laser fluence and spot size at the surface of the target have a significant effect on the stoichiometry of the ablated elements. In the PLD system used in this study, the laser intensity and the spot size are controlled by optical attenuators and a convex lens. The optical attenuators are placed in front of the laser source (not shown in Fig. 2.1 (a)) and the distance from the target surface to the convex lens is adjustable. The top of the target is placed at a defocusing

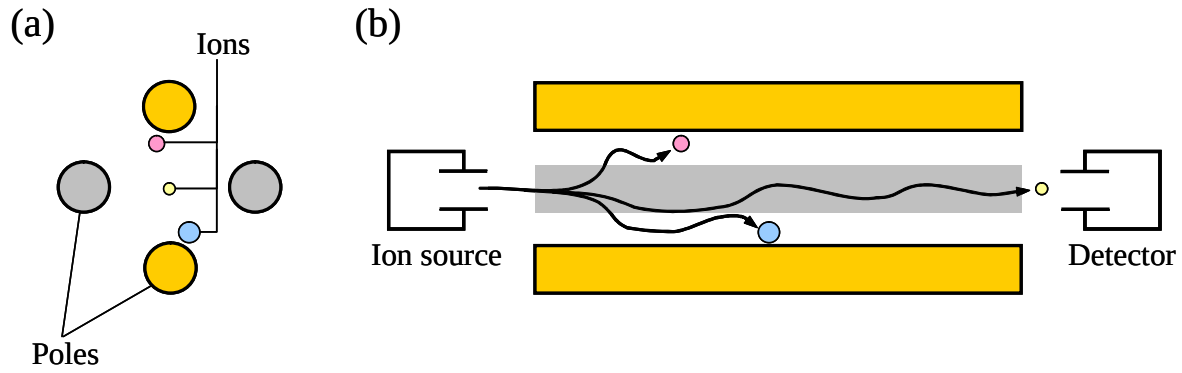

Figure 2.3: Schematic (a) cross section and (b) horizontal section of the Qmass. The different colors indicate the different ion masses. Opposite poles are electrically connected (yellow-yellow and gray-gray).

position (between the focal position and the imaging position). The ablated area has a square shape, the size of which can be modified by changing the focal length as shown in Fig. 2.2 (a) and (b). Generally, the expansion of the plume tends to be larger as the spot size decreases. The relationship between the spot size and the convex lens position has been investigated as shown in Fig. 2.2 (c). When the spot size becomes smaller, the blurred edges of the spot become relatively large, making an accurate determination of the spot size difficult. For that reason, in this study, the extrapolated values are taken in the small spot size region.

2.1.3 Ozone and quadrupole mass spectroscopy

Ozone is utilized in our PLD system as a strong oxidation source. The purpose, set up, and usage will be described in the following Chapter.

In order to confirm the existence of ozone, a quadrupole mass spectrometer (Qmass) (Dycor^{TM} LC200MS: AMETEK Inc.) is attached to the main chamber as illustrated in Fig. 2.1 (a). The Qmass is composed of four electrical poles as shown in Fig. 2.3. Two pairs of opposite facing poles are connected. In each pair of poles, a direct current passes and an alternating electrical field with high frequency is applied. When ions pass through the center of the four poles, they are perturbed depending on their ion mass. As a result, only an ion with a particular mass can reach the detector, while other ions are trapped by the poles. By controlling the ratio and the intensity of the direct current and the alternating electrical field, ions with different masses can be detected independently.

In this PLD system, the quantity of Oxygen atoms O (atom weight: 16), Oxygen molecules O_2 (32), and Ozone O_3 (48) is monitored when the ozone generator is operated. Since the operating pressure range is from ultrahigh vacuum to 10^{-4} Torr, the existence of ozone has been confirmed below 10^{-4} Torr. However we often utilize ozone above 10^{-4} Torr, meaning that we cannot confirm the quantity of O_3 in this regime.

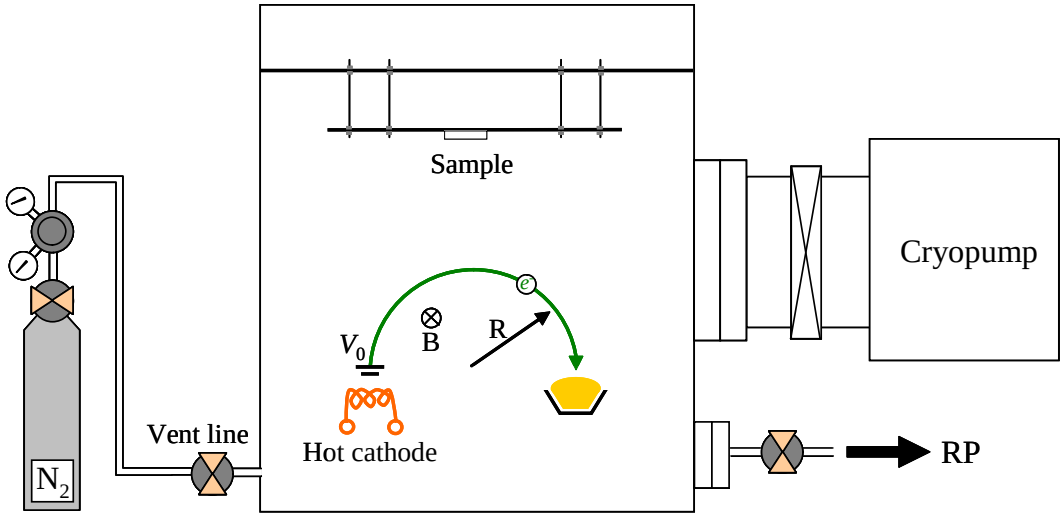

Figure 2.4: Schematic illustration of the metal evaporator.

2.1.4 Ohmic contact

After preparing a sample, ohmic contacts are fabricated to measure the transport properties. In this study, gold and aluminum contacts were used. Both contacts are fabricated in a metal evaporator as shown in Fig. 2.4. The base pressure is about 10^{-5} Torr. Usually, the thickness of contact is set around 500 Å.

In the case of making gold contacts, a gold target in a carbon crucible is heated by thermal electrons from a hot cathode, and then evaporated to the sample placed facing the crucible at the top of the chamber. Electrons from the cathode are extracted by an accelerating voltage V_0. Then, the magnetic field B from the permanent magnet bends the orbit of the electrons towards the gold target. From the balance between the centrifugal force and the electromagnetic force, their orbital radius R can be calculated,

$$\frac{me \cdot v^2}{R} = evB. \qquad \therefore R = \frac{\sqrt{2mV_0}}{B} \tag{2.1}$$

where m is the mass of electron, v is the velocity of electron, and the relationship of $\frac{mv^2}{2} = eV_0$ is taken into account. The orbital radius R can be modified by the change of the accelerating voltage $V_0 = 4$ kV and the magnetic field B. In this system, V_0 is used as a tuning parameter since B is constant.

In the case of making aluminum contacts, aluminum is resistively heated inside a tungsten boat and evaporated in the same evaporator.

2.2 Characterization of basic physical properties

2.2.1 Surface morphology

Surface morphology is one of the important thin film properties which reflects the quality of the sample. A flat surface indicates homogeneous growth from the interface to the

top surface. On the other hand, particles and precipitates on the surface often provide important information reflecting the film off-stoichiometry and the growth mechanism. In this study, the surface morphology is characterized by an atomic force microscope (AFM: Veeco, Digital Instruments Dimension^{TM}). The AFM is one method to directly observe the surface utilizing Van der Waals forces between the sample and the tip. The tip is located at the end of a cantilever, which is oscillated by a piezoelectric device. The oscillation is monitored by a laser which is reflected off the cantilever. When the Van der Waals force is changed, the cantilever oscillation is also modulated. The surface structure is primarily detected as the change in the force experienced by the tip, and then converted into voltage. By scanning a specified area, we can obtain 3D surface information.

2.2.2 Crystal structure

X-ray diffraction (XRD) is a widely used method to determine the crystal structure of thin films, because the wavelength of x-rays and the atomic spacing in the crystal are of the same order. A high resolution XRD system (D8 Discover: Brucker AXS Inc.) is employed in this study. The samples were irradiated by Cu Kα_1 radiation (λ=1.54056 Å) which was monochromated by a Ge (220) monochromator. Three types of measurement are mainly made: θ-2θ scans, rocking curve, and reciprocal space mapping (RSM). θ-2θ scans give us information about the film epitaxy and lattice spacing perpendicular to the substrate, as calculated by Bragg's law. The full width at half maximum (FWHM) of the rocking curve gives information about the crystallinity of the film. From RSM, we can deduce the in-plane lattice constants. Based on information about the crystal structure of the films, we can discuss the difference from bulk propeties and consider the correlation between the crystal structure and other physical properties.

2.2.3 Thickness measurements

In this study, the film thicknesses have been determined by three different methods: a stylus profilometer, thickness fringes of the XRD peaks, and Sherrer's equation. The appropriate method was selected depending on the thickness and the crystallinity of the films.

As a stylus profilometer, a Dektak® 6M Stylus Profiler (Dektak) (Veeco Instruments Inc.) was used. By measuring across the edge between the film and the bare substrate, [1] the film thickness is measured directly. The Dektak is suitable for relatively thick films so that it was used when the expected film thickness was over 500 Å.

When out-of-plane coherent growth is achieved, we can observe several fringes around the Bragg peaks in the θ-2θ measurement. We can derive the film thickness t using,

$$t = \frac{\lambda}{2(\sin\theta_{n+1} - \sin\theta_n)}, \tag{2.2}$$

[1] When fabricating the thin film, the edges of substrate are clamped to secure the sample. Thus, the target material is not deposited onto the clamped edges.

where λ is the wavelength of the Cu Kα_1 line (λ=1.54056 Å), and $\sin\theta_n$ and $\sin\theta_{n+1}$ are the neighboring angles.

The FWHM of the film Bragg peaks also gives useful information about the film thickness. Sherrer's equation, which was originally a method to calculate the size of crystal domains, can be used as a method to estimate the thickness of relatively thin films because the size of crystal domains can be approximated to be of the same order as the film thickness. From Bragg's law, we multiply both sides by an integer m such that $md = t$, giving

$$m\lambda = 2t\sin\theta. \tag{2.3}$$

Next, we differentiate both sides of Eq. (2.3) remembering $m\lambda$ is a constant,

$$0 = 2\Delta t\sin\theta + 2t\cos\theta\Delta\theta, \tag{2.4}$$

then,

$$t = \frac{\Delta t\sin\theta}{\cos\theta\Delta\theta}. \tag{2.5}$$

Since the smallest increment in t is d, using $\Delta t = d$, and substituting $\lambda/2$ for $d\sin\theta$ (from Bragg's law) we get,

$$t = \frac{\lambda}{2\cos\theta\Delta\theta}. \tag{2.6}$$

A more sophisticated analysis of the problem gives a prefactor of 0.9 on the right hand side of Eq. (2.6) and leads to Scherrer's equation,

$$t = \frac{0.9\lambda}{2\cos\theta\Delta\theta}. \tag{2.7}$$

Thus, if the FWHM is used as $\Delta\theta$, we can simply calculate t.

2.2.4 Transport properties

In-plane transport properties of thin films are measured by a standard four-probe measurement. After making ohmic contacts, metal wires (Au wires are used in most cases) are attached by hand onto the contacts of the sample with Ag paste. The measurement is carried out using the resistance bridge of a Physical Properties Measurement System (PPMS: Quantum Design Co.). In the PPMS, we can measure transport properties with continuously changing temperature, and a superconducting magnet also allows a magnetic field to be applied. The utilized range of temperature was from 2 K to 300 K, and magnetic field between ±8 T.

2.3 Characterization of junction properties

2.3.1 Current-voltage and capacitance-voltage characteristics

Standard current - voltage (I-V) and capacitance - voltage (C-V) characteristics are measured across the junctions. Both of the detailed theories are not described in this

thesis, but can be found elsewhere [15]. I-V measurements were carried out in the PPMS using a Semiconductor Parameter Analyzer (SPA: Agilent Technologies, Inc.) or Sourcemeter (Keithley 2410). C-V measurements were also investigated in PPMS with a Precision LCR Meter (LCR Meter: Agilent Technologies, Inc.). Detailed measurement parameters will be described in each Chapter.

2.3.2 Photovoltaic measurement

In order to realize photocarrier injection (PCI) in these samples, ultra-violet light is required. As a light source, a LAX-102 (Asahi Spectra Co., Ltd.) is used. The emitted light from a Xe lamp is reflected by mirrors to provide a specific range of wavelength. In our system, the range of ultra-violet light, 300 $\sim$ 400 nm, is selectively transmitted. To control the light intensity, 1 % and 12 % attenuators were used.

Since photovoltaic measurements are carried out in the PPMS, a fiber bundle and an imaging lens system were previously designed and could be installed into the sample space of the PPMS. An overview of the set up is shown in Fig. 2.5. The maximum intensity we can achieve is 25 mW/cm^2. By using a neutral density (ND) filter, we can digitally modify the light intensity from 1 % to 100 %. In addition, we can select the wavelengths at 10 nm intervals from 310 $\sim$ 380 nm by using the band-pass filters.

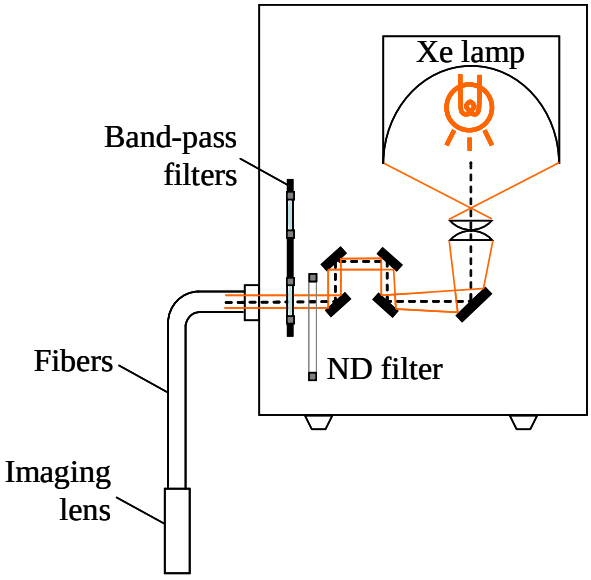

Figure 2.5: Schematic overview of the optical system using in the photovoltaic measurements.

Chapter 3

Ozone

3.1 Advantages of ozone utilization

An ozone generator has been installed for use with our PLD chamber. Here many strong advantages of the use of ozone in the growth of oxide films will be introduced.

First, the oxidizing power of ozone has a large effect on the growth of oxide films. It is known that ozone is the second strongest oxidizing agent after fluorine [16] and its oxidizing power is higher than that of the molecular oxygen by a factor of more than 10^6 [17]. According to other reports, it is said that the activity of ozone at $T = 300$ K is 10^{19} times larger than that of molecular oxygen [18, 19]. Because the physical properties of oxides can be easily changed by the existence of an oxygen deficiency, a sufficient supply of oxygen is essential in the growth of oxide films. In addition, powerful oxidization potentially serves to stabilize new phases, which we cannot access with molecular oxygen. For example, $SrFeO_3$ thin films are unstable under conventional PLD conditions (and can be stabilized only under oxygen pressures as high as ~ 50 MPa), but epitaxial thin films were successfully fabricated under an ozone atmosphere [20].

Ozone can be utilized for surface treatment of substrates as well. Due to the strong oxidization power, carbon contamination can be easily removed at relatively low temperatures. Clean surfaces without contamination are highly important for achieving good properties of interfaces and junctions. In ultra-thin films, the interface condition has a crucial effect on the film properties [21]. As for junction properties, there is a report that ozone enhances the rectification properties in Schottky junctions [22].

The leading reason why we utilize ozone in our PLD chamber is that it can enhance the superconducting properties of $La_{2-x}Sr_xCuO_4$ thin films [11, 17, 23]. By utilizing ozone during thin film growth, we can obtain higher T_c than bulk [17, 23]. In addition, we can make superconducting $La_2CuO_{4-\delta}$ [11], which is an insulator in the bulk phase.

In this Chapter, the set up of ozone generator in our PLD chamber will be overviewed after briefly introducing the basic characteristics of ozone. Finally, we will show the confirmation of the existence of ozone in the chamber.

3.2 Overview of ozone characteristics

In the normal atmosphere, the concentration of ozone is 0.005 ppm. Ozone is well known as an absorber of ultra violet light in the ozone layer. Due to its high reactivity, about 95 % of ultra violet light from the sun is absorbed in this layer.

Ozone O_3 is a resonance hybrid

$$O^- = O^+ - O \qquad \rightleftharpoons \qquad O = O^+ - O^-, \tag{3.1}$$

which is unstable and can be easily decomposed into molecular oxygen O_2. The decomposition of ozone is a function of temperature and the concentration of O_2. In general, the half-life is a few seconds at 200 °C in air as a consequence of the high oxidization power [16].

There are three main generation methods of ozone: the photochemical reaction method, the electrolytic method, and the discharge method. The first method utilizes the photochemical reaction between O_2 and ultra violet light

$$O_2(g) \xrightarrow{\text{UVlight}} 2O^{\bullet}, \tag{3.2}$$

$$O_2(g) + O^{\bullet} \longrightarrow O_3(g). \tag{3.3}$$

The dissociation reaction of O_2 (Eq. 3.2) proceeds under the wavelength of 185 nm [16]. However, ultra-violet light of wavelength 254 nm decomposes O_3 into O_2

$$O_3(g) + O^{\bullet} \xrightarrow{\text{UVlight}} \frac{1}{2}O_2(g). \tag{3.4}$$

Because ultra-violet light generates and decomposes ozone at the same time, we cannot obtain a high-concentration of ozone by this method. The second method decomposes H_2SO_4 aq. or HCl aq. by electric currents. Because it requires extremely large currents, it is not suitable for practical use. Finally, the discharge method is the most widely used. If we apply high voltage to O_2 gas, O_2 can transform into O_3. There are three types of discharge: silent electric discharge, corona discharge, and combined discharge. In this study, we used silent electric discharge.

Since ozone is a toxic gas, excess ozone gas needs to be decomposed before exhausting to air. In this set up, we used the heating method and carbon adsorption to decompose excess ozone. When temperature increases, the dissociation process of O_3 is accelerated. The carbon adsorption method is steady and effective to break down ozone. When ozone is adsorbed on the surface of carbon, it reacts with carbon and produces CO_2 and a small volume of CO. This process is exothermic [16],

$$2O_3(g) \longrightarrow 3O_2(g) + 286\text{kJ/mol}. \tag{3.5}$$

The activation energy of this process is large, so the reaction rate is not fast [16]. Additionally, ozone accumulates on the surface of carbon, so the carbon must be exchanged.

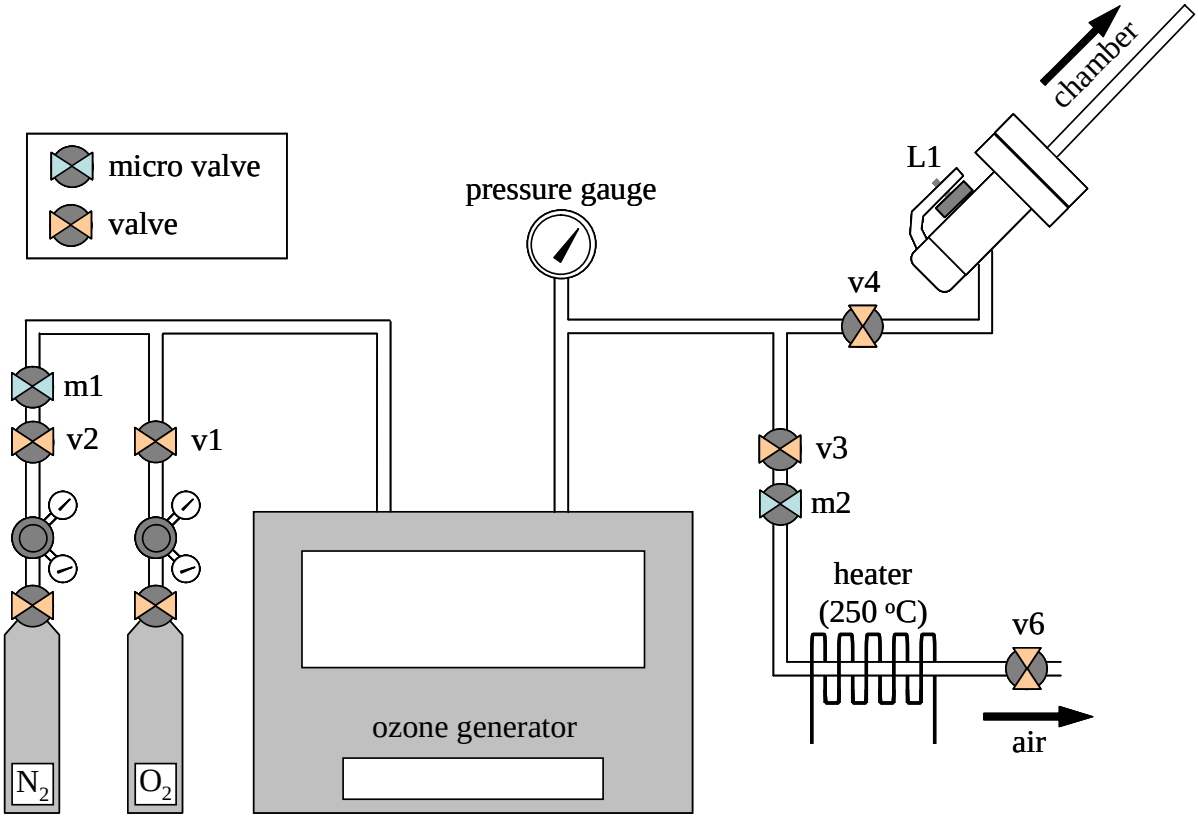

Figure 3.1: Schematic illustration of the set up of the ozone generator. The central grey box represents the main component. The frequently used valves and micro valves are labeled. L1 is a variable leak valve, which directly connects to the main PLD chamber. v6 valve is open to the atmosphere. The pressure in this system can be monitored by the pressure gauge. N_2 gas is installed to enhance the O_3 generation rate.

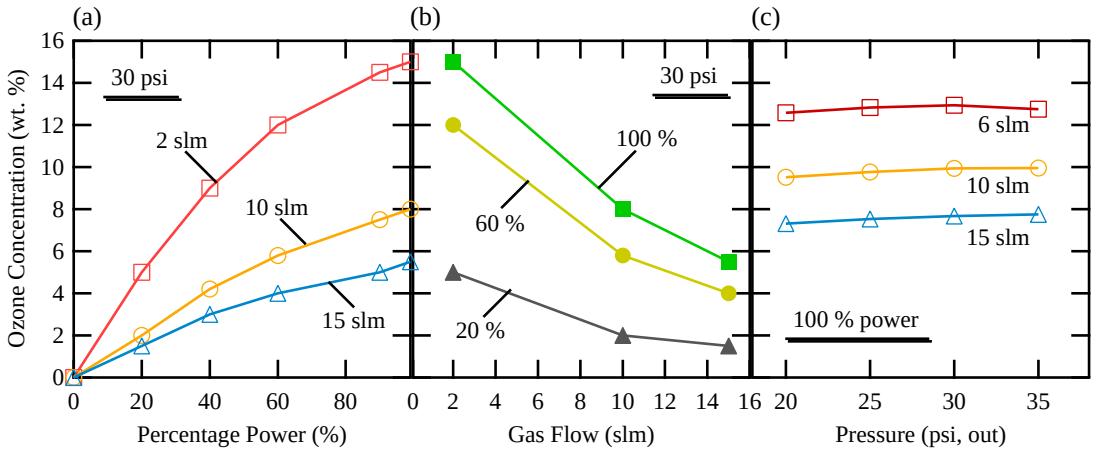

Figure 3.2: Ozone concentration in the output gas as a function of (a) output power (%), (b) gas flow through the ozone generator, and (c) gas pressure inside the ozone generator.

3.3 Installation of the ozone generator

As the ozone generator, SEMOZON® AX8401 (MKS Instruments, Inc.) was used. Ozone is produced from oxygen by electrical discharge inside the ozone-generating cells. The cell can be represented as a parallel-plate capacitor. Oxygen flows between the electrodes, where we apply the voltage which generates an oxygen plasma. Ozone is produced as a result of oxygen ionization.

The overview of the system is shown in Fig. 3.1. It can be divided into four parts: oxygen source, ozone generator, inlet to the chamber, and the exhaust to the atmosphere. We use Grade 6 oxygen as the oxygen source. Controlling the pressure inside the ozone generator by the regulator, oxygen flows into the ozone generator from the cylinder. As a promoter, 100 ppm N_2 gas is also added. Applying a high voltage to the flowing gases, some parts are converted into ozone. The output is a mixture of O_2 and O_3. The mixture gas goes into the main chamber through the variable leak valve (L1), and is exhausted to the atmosphere via the heated tube and valves. The temperature of the heater is around 250 °C, which is enough to decompose O_3 into O_2.

The pipes where oxygen and ozone pass through were made of SUS304. The inside of pipes ozone passes was electrically polished and the pipe joints were fastened with VCRs. As for the part of pipes where the exhasut gas passes, Teflon® was used. We used the Au-coated copper gaskets to seal the connections where ozone passes, instead of the gaskets of oxygen free high conductivity copper. This is to prevent the gaskets from deteriorating under the strong oxidization of ozone. The gaskets of oxygen free high conductivity copper, which are utilized in usual, are easily oxidized to copper oxide by ozone, resulting in decomposing ozone. In the same reason, we exchanged the copper gascket used in L1 for the alminum one, which was fabricated with the help of Mr. Saito.

The ozone concentration in the output gas is determined by three parameters: the

output power (voltage applied to the cell), the gas flow, and the gas pressure. The output power can be tuned manually by turning the potentiometer on the front panel of the ozone generator. The gas flow depends on the flows through the valves v1, L1 and m2 (Fig. 3.1). The gas pressure is determined by the pressure of the O_2 cylinder. In accordance with the intended use, we should tune each parameter. In this study, we carried out under the output power of 100 %, the gas flow of 2 slm, and the pressure of 23 psi. As shown in Fig. 3.2, a mixture of 10 % ozone and 90 % molecular oxygen can be supplied in this condition.

3.4 Confirmation of the existence of ozone

Ozone is an invisible gas without any color, and has a very irritating odor which is dangerous to inhale. In order to confirm the existence of ozone from L1, we performed two different tests. One test utilizes the chemical reaction of potassium iodide (KI). Ozone is a strong oxidant so that KI is easily reduced. When KI is reduced, the color changes as shown in Fig. 3.3 (a). Another is the use of a quadruple mass spectrometer (Qmass; see §2.1.3) to give a more quantitative measure of the ozone generation. We can see the increase of the amount of ozone at the time of 130 s as indicated by the allow in Fig. 3.3 (b). By both methods, we could successfully confirm the production of ozone.

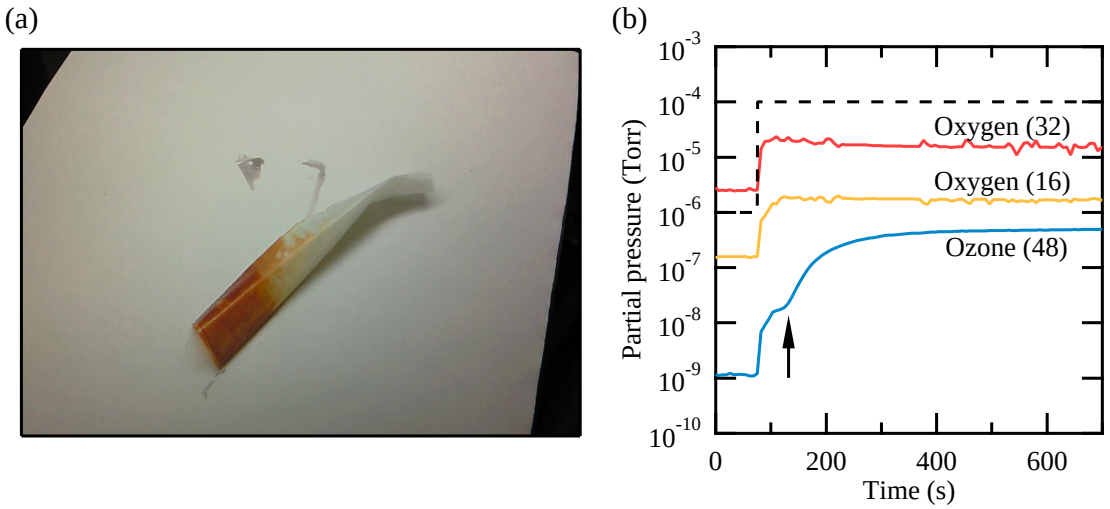

Figure 3.3: (a) Photograph of paper previously immersed in KI solution (15 %), which is reduced by ozone resulting in the change of color. (b) Partial pressures measured by Qmass. The dashed line indicates the nominal value measured by the ion gauge equipped in the main chamber. The allow indicates the point that ozone starts to increase in the main chamber.

Chapter 4

Crucial T_c determinants in the $La_{2-x}Sr_xCuO_4$ system

4.1 High-T_c superconductors

The great discovery in 1986 by J. G. Bednorz and K. A. Müller opened up the new research field of high-T_c superconductors [1]. More than 20 years have passed and there are over 100,000 articles related to high-T_c materials [24]. The mechanism of high-T_c superconductors is still controversial and the initially rapid increase in the superconducting temperature T_c has stagnated recently. There is also no unified explanation to clarify the key parameters needed to realize d-wave Cooper pairs. As for the T_c, after achieving a highest superconducting temperature T_c of 135 K in 1993 [25] (164 K under high pressure [26, 27]) in $HgBa_2Ca_2Cu_3O_{8+\delta}$, no other materials exceeding this value have been found since.

In spite of the unclear mechanism, all of the high-T_c superconductors have a common feature that they all have the CuO_2 planes. As shown in Fig. 4.1, the Cu $3d$ orbital and O $2p$ orbital are strongly hybridized so that a CuO_2 plane forms a square grid. The spins of the Cu^{2+} electrons are localized at each Cu atom and ordered antiferromagnetically due to the strong correlations [2]. When CuO_2 planes are doped from the reservoir layers

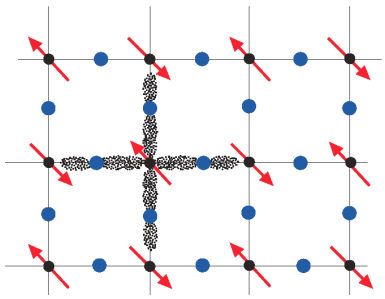

Figure 4.1: Schematic of a CuO_2 plane [12]. Black and blue closed circles represent copper and oxygen atoms, respectively. Red allows indicate the direction of the electron spins localized on the copper atoms, which order antiferromagnetically. Cu $3d$ and O $2p$ orbitals are strongly hybridized as depicted by the gray clouds.

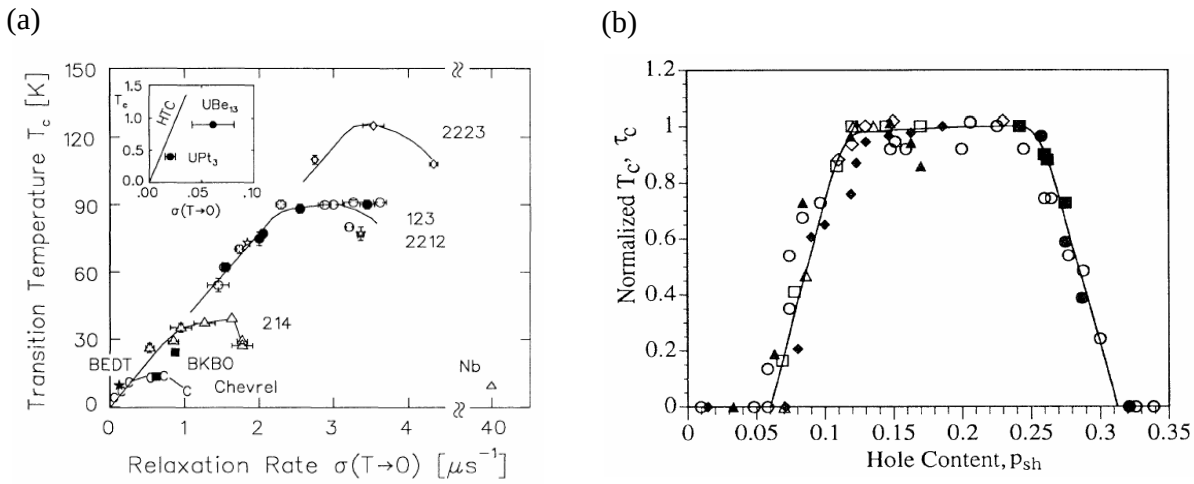

Figure 4.2: (a) Plots of T_c as a function of $\sigma(T \rightarrow 0) \propto \rho_s$ (see Ref. [29] for details), underdoped high-T_c cuprates are well fitted on the Uemura plot. (b) The universal relationship between $\tau_s = T_c/T_{c,max}$ and the hole content per CuO_2 plane ρ_{sh}, as claimed in Ref. [30].

which sandwich a CuO_2 layer(s), the localized electrons become itinerant. Then, they form d-wave Cooper pairs on the CuO_2 planes [28].

The platform of high-T_c superconductors is the CuO_2 planes, which essentially the same in the whole family of cuprate superconductors. In this sense, T_c is supposed to be defined only by the amount doping in the CuO_2 layers. It is, however, not the case. T_c strongly depends on the materials, ranging from 30 K to 135 K, even though all superconducting properties originate from the same CuO_2 planes. This indicates that parameters other than just the CuO_2 planes have strong effect on T_c. Actually, there are many reports concerning other parameters which can determine T_c, many of which are related to the crystal chemistry. An understanding of the T_c determinants will give many strategies to enhance T_c. Furthermore they may unveil the mechanism of high-T_c superconductivity.

In this Chapter, the crucial T_c determinants will be introduced. First of all, we will start from the clean limit of the high-T_c superconductors. Important factors for the enhancement of T_c will be discussed in this regime. Based on this clean limit, what occurs as we deviate from this limit will be reviewed next. We will mainly focus on the properties of $La_{2-x}Sr_xCuO_4$ thin films.

4.2 The chemically clean limit

It is important to know how T_c responds to perturbations in the clean limit. High-T_c superconductors intrinsically include many impurities because they inevitably require the carrier doping by chemical substitution [28]. Strictly speaking, there are no high-T_c superconductors without impurities. In order to avoid confusion, we define the clean

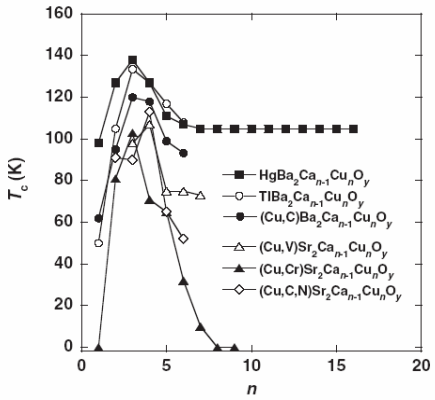

Figure 4.3: Relationship between T_c and the consecutive number of CuO_2 planes n [32]. In all systems, T_c reaches a peak at $n = 3$.

limit as materials maintaining stoichiometry of the chemical formula. We distinguish the intentional impurities needed for carrier doping from the unintended impurities, some of which strongly suppress T_c. In this clean limit, we can summarize three important factors for the enhancement of T_c: (i) the carrier concentration in the CuO_2 plane, (ii) to make the CuO_2 planes clean in terms of flatness and chemical purity to avoid scattering Cooper pairs, (iii) to keep the CuO_2 plane as far away from the reservoir layers as possible.

As for the relationship between T_c and the carrier concentration, it was pointed out that high-T_c superconductors empirically follow two universal scaling laws. First is that T_c increases in proportion to the superfluid density ρ_s, which is strongly connected to the doped carrier concentration. Even though it is limited to the underdoped region, it can be said that T_c is a linear function of the carrier content as shown in Fig. 4.2 (a). This is called the Uemura plot [29]. Above a certain threshold in the carrier concentration, T_c saturates, and is then suppressed. As a second characteristic, this behavior of having a maximum can be scaled for different materials. As shown in Fig. 4.2 (b), the phase diagram of T_c versus number of carriers per CuO_2 plane x is known to form a bell-shaped curve rising from $x \approx 0.05$, then increasing in proportion to the carrier content, and eventually dropping at $x \approx 0.3$ after saturating at around $x \approx 0.175$ [30, 31]. Practically, the amount of dopant carriers and the absolute value of T_c depend on the system. In this way, T_c can be understood as a function of carrier content.

The number of consecutive CuO_2 planes n is another key parameter for the enhancement of T_c. It is empirically known that T_c reaches a peak at $n = 3$, and starts to decrease for $n \geq 4$. This has been investigated both from the experimental side [32] and the theoretical side [31]. In order to understand this trend, the *inner* CuO_2 plane which is sandwiched by two CuO_2 planes is of key importance. It is known that the *inner* CuO_2 plane is more flat and clean than the *outer* planes which lie next to the reservoir layers, and contain many dopant impurities [28]. The distance between the CuO_2 planes and the reservoir layers is also important. For increasing T_c, it is better that this distance is long. As the distance becomes longer, the disorder effect of the reservoir layer on the

CuO_2 plane gets smaller. In addition, $HgBa_2Ca_2Cu_3O_{8+\delta}$, which shows the highest T_c so far, has the longest distance between these layers [25, 28]. On the other hand, the reason why T_c decreases as n exceeds 4 is the insufficiency of dopant carriers in the *inner* plane because the distance becomes too far from the reservoir layer [28].

Based on the above criteria, we can see three directions to enhance T_c. The first is to optimize the carrier content on the CuO_2 plane. It is important to optimize the amount of chemical substitution. Then, we need to exclude the factor which suppress superconductivity in the CuO_2 planes, namely disorder and interference. Although making multi-layered CuO_2 planes is one representative idea, the basic concept is to make CuO_2 plane flat, clean, and separated from the reservoir layers. We can confirm these points from the resistivity and the lattice length perpendicular to the CuO_2 plane.

4.3 $La_{2-x}Sr_xCuO_4$

4.3.1 Correlations between T_c, c-axis, and resistivity

The phase diagram of bulk $La_{2-x}Sr_xCuO_4$ has been widely investigated [8]. The representative behavior of resistivity and superconducting transition temperature T_c is shown in Figs. 4.4 (a) $\sim$ (d). [1] Here, one Sr^{2+} substitution produces one hole in the CuO_2 plane. In bulk, the amount of substitution is the only controllable parameter, in other words, it decides all the physical properties as long as stoichiometric composition is maintained. The behavior of the resistivity for each Sr^{2+} dopant changes as follows. When $x \leq 0.05$, it is insulating. Due to the strong electron-electron interaction, it is still an antiferromagnetic Mott insulator [2]. In the range of $0.05 \leq x \leq 0.25$, superconductivity appears. As seen in Fig. 4.4 (b), the optimal doping content is around $x \sim 0.15$, where T_c increases up to ~ 40 K. We can also see the low temperature upturn of the resistivity at $x = 0.06$ (N.B. it is written as $x = 0.03$ in Fig. 4.4 (b)), even though eventually it undergoes a superconducting transition. This upturn is often observed in the underdoped region and in thin films, and is due to variable range hopping (VRH) [33, 34]. This indicates the imperfections of Cooper pairs in the CuO_2 plane due to the insufficiency of the dopant concentration or the existence of impurities. At $x \geq 0.25$, superconductivity disappears. In this range, it becomes a Fermi liquid.

The crystal structure has a one-to-one correspondence with the amount of Sr. As shown in Fig. 4.4 (e), in-plane a-axis length shrinks and out-of-plane c-axis length extends as the Sr content increases. In addition, the behavior of the low temperature resistivity also has a one-to-one correspondence with the amount of Sr. We can therefore estimate the physical properties at low temperature from the room temperature resistivity. T_c can be scaled with axis length and resistivity. Although the absolute values of the lengths and the resistivity show some variation, the correlation can be always observed in a systematic

[1] The method of defining x in Fig. 4.4 and the main text is different. In the text, we use only the $La_{2-x}Sr_xCuO_4$ form.

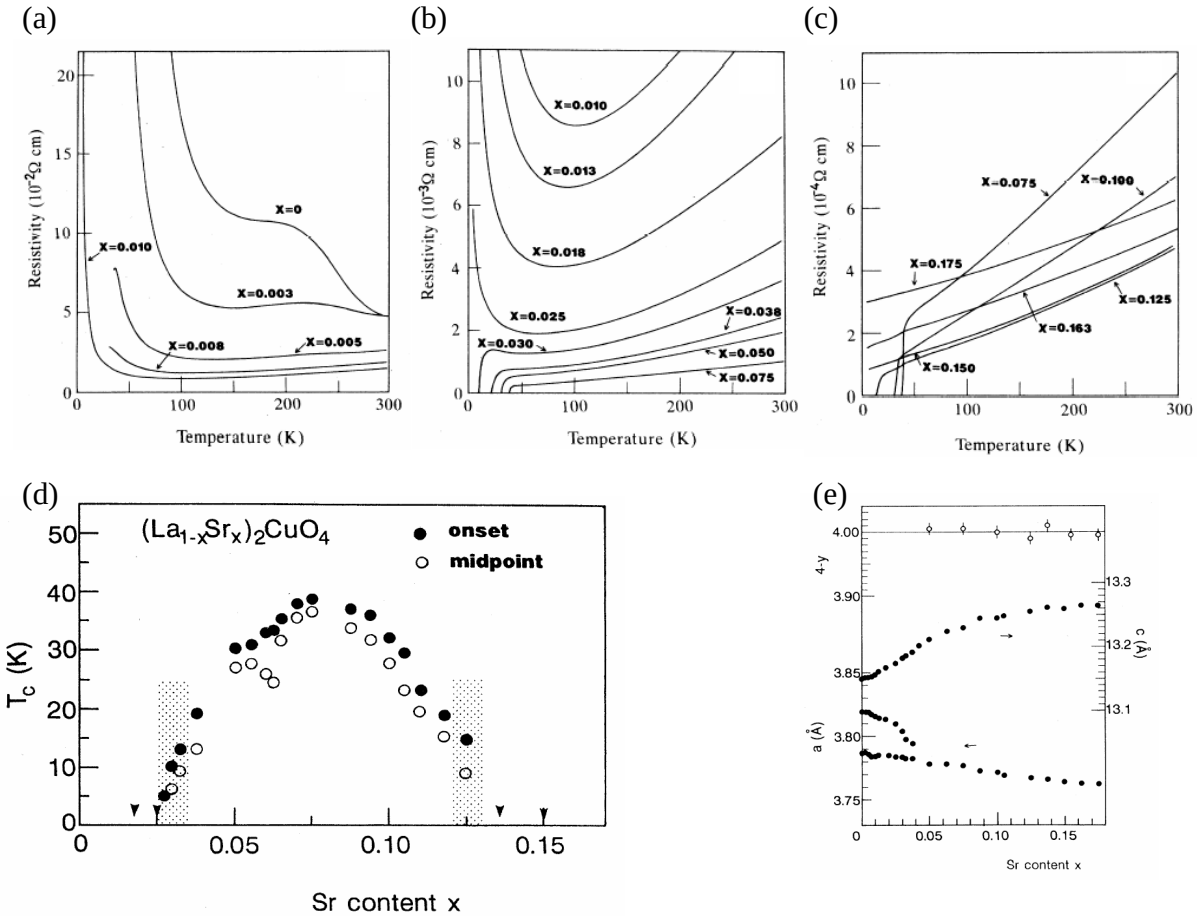

Figure 4.4: (a) $\sim$ (c) The resistivity as a function of temperature, (d) the phase diagram and (e) lattice lengths as a function of Sr content in the $(La_{1-x}Sr_x)_2CuO_4$ system [8]. In (e), y corresponds to the oxygen vacancy concentration in $(La_{1-x}Sr_x)_2CuO_{4-y}$.

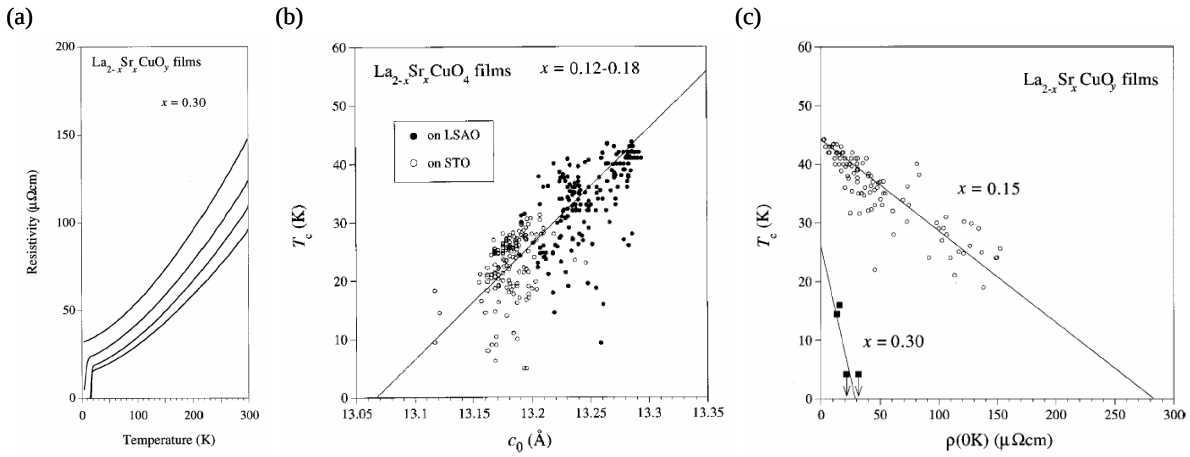

Figure 4.5: (a) Temperature dependence of the resistivity in $La_{1.7}Sr_{0.3}CuO_4$ samples grown on $LaSrAlO_4$ under the same conditions. (b) Plot of T_c with the c-axis length (c_0) for $La_{2-x}Sr_xCuO_4$ thin films with $x = 0.12$ to 0.18. The thickness of the films ranges from 150 to 4500 Å. Closed and open symbols are for films on (001) $LaSrAlO_4$ and (100) $SrTiO_3$ substrates, respectively. The solid line represents the result for a linear fit to the data points. (c) Plot of T_c with $\rho(0\ \mathrm{K})$ for $La_{2-x}Sr_xCuO_4$ thin films on (001) $LaSrAlO_4$ substrates. The thickness of the films ranges from 150 to 4500 Å. Open and closed symbols are for the films with $x = 0.15$ and 0.30, respectively. The solid lines represents the results of linear fits to the two data sets. These data are taken from Ref. [23].

bulk system.

On the other hand, this one-to-one correspondence between T_c, resistivity, and lattice constants is not true in thin films. If we fix the Sr content, we cannot obtain the intended physical properties with respect to the bulk phase diagram, as shown in Fig. 4.4 (d). T_c is often lower than the bulk, the c-axis is shorter, and the resistivity is higher. The superconductivity can be easily suppressed in the case of thin films. This is due to two *intrinsic* differences between bulk and thin films: lattice mismatch and thickness.

As shown in Fig. 4.5 (a), the behavior of the resistivity and T_c vary widely even though every film has the same chemical composition and is grown on the same substrate. It potentially occurs that, in thin films, the physical properties changes as if dopant content changed, even though we actually keep it constant during fabrication. There are fortunately clear correlations between several physical parameters. By comparing them carefully, we can discuss and eventually predict the superconducting properties from other physical parameters.

It is well known that longer c-axis increases T_c. The correlation has been investigated as shown in Fig. 4.5 (b). The c-axis length changes not only when we fabricate films on substrates formed of different materials, but also when we use the same substrate and vary other parameters. In both cases, however, the correlation works. In addition, this can be seen in other high-T_c superconductors. It can be said that this correlation is universal, and originates from the mechanism of high-T_c superconductivity. The strong correlation between T_c and resistivity is also often pointed out. We can see that as the

resistivity at room temperature increases, T_c decreases and eventually disappears even though all of the films have the same Sr content. As shown in Fig. 4.5 (c), there is a negative linear correlation between T_c and resistivity.

T_c scaling with c-axis and resistivity at room temperature are both universal. This can be understood as analogies we have seen in the clean limit in §4.2, which are that it is important to make the CuO_2 plane flat, clean, and positioned away from the reservoir layers. For the $La_{2-x}Sr_xCuO_4$ thin films, it is required to obtain the film which has low resistivity and a long c-axis.

There are, however, many ways to change the c-axis and resistivity. In other words, c-axis and resistivity are phenomena with many origins. For example, the c-axis and resistivity depend on the film thickness. Actually, data shown in Figs. 4.5 (b) and (c) come from samples with different thicknesses. Impurities also affect the c-axis and resistivity. We need to clarify the fundamental origins that can change these parameters.

4.3.2 Thickness

One of the central concerns about high-T_c superconductors is the minimum thickness required for superconducting properties to appear. It is a fundamental question how many CuO_2 planes are needed to realize high-T_c superconductivity. Basically, the fabrication of thin films is getting more difficult as the thickness becomes thinner because superconductivity abruptly disappears in the thin region, as shown in Figs. 4.6. However, the thin limit where T_c appears is still controversial. So far, appearances of superconducting property in a 2-unit-cell film of $La_{1.85}Sr_{0.15}CuO_4$ [36], in a one-unit-cell film of $La_{1.9}Sr_{0.1}CuO_4$ with buffer and cap layers [37], and in a single CuO_2 plane embedded in a bilayer combining insulating La_2CuO_4 and metallic $La_{1.55}Sr_{0.45}CuO_4$ [9] were reported.

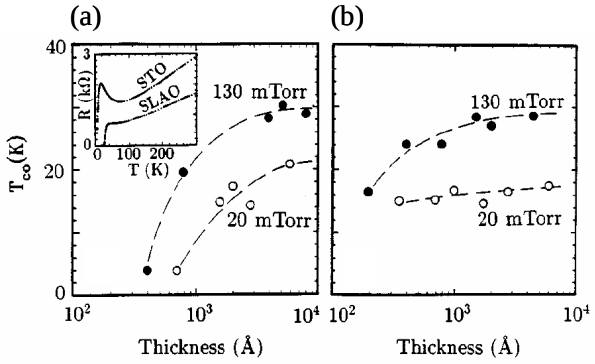

Figure 4.6: Thickness dependence of the T_c for two different oxygen pressures for films deposited on (a) $SrTiO_3$ (001), and (b) $LaSrAlO_4$ (001) substrates [35]. Inset: R(T) for two similar films with thicknesses of 400 Å, deposited on $SrTiO_3$ and $LaSrAlO_4$ substrates.

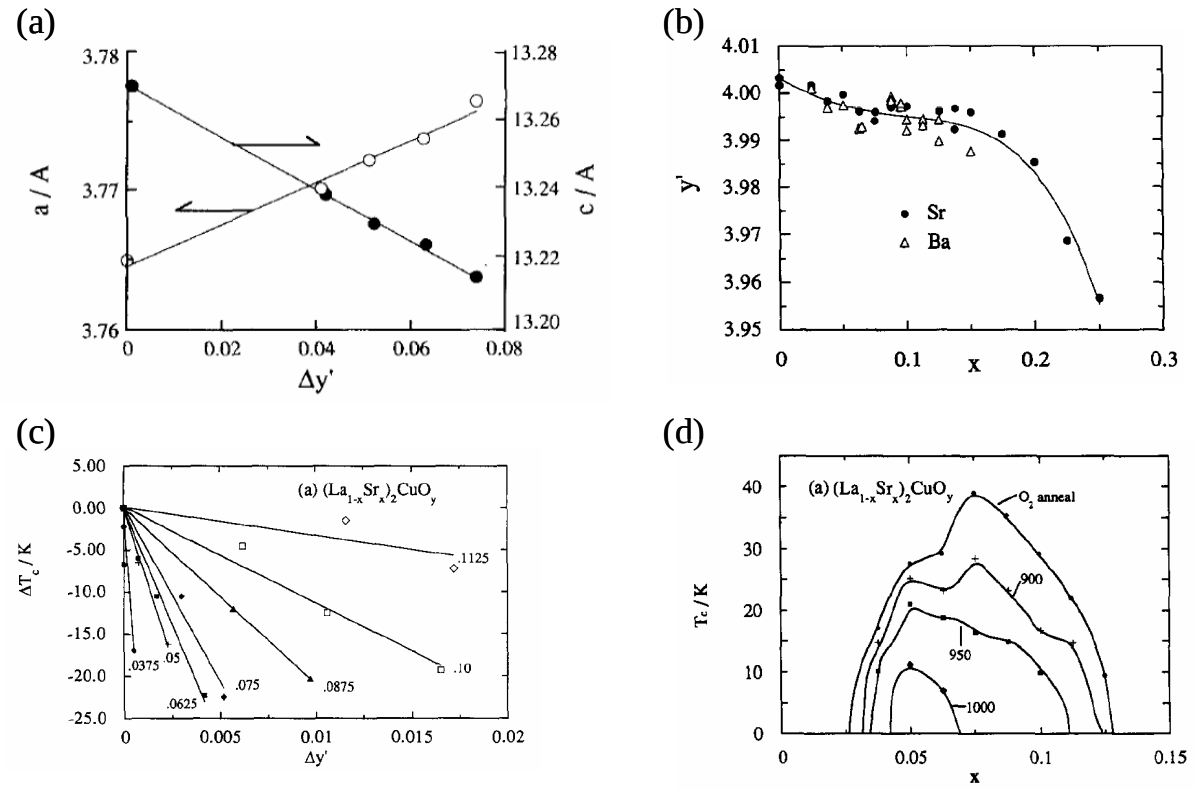

Figure 4.7: Data taken from Ref. [38] are displayed. x and Δy are corresponding to the amount of Sr and oxygen deficiency in the chemical composition of $(La_{1-x}Sr_x)_2CuO_{4-\Delta y}$. (a) a- and c-axis lengths as a function of Δy ($La_{1.7}Sr_{0.3}CuO_{4-\Delta y}$). (b) The maximum amount of oxygen deficiency at each x. (c) Decrease of T_c as a function of Δy. (d) Variation of T_c as a function of x under several annealing conditions.

4.3.3 Oxygen deficiency

In cases where the chemical composition deviates from $La_{2-x}Sr_xCuO_4$, the universal correlation collapses. This also brings about phase segregation. However, the crystal can hold its structure and its physical properties to some extent when the deviation is relatively small. One such deviation is oxygen vacancy formation. Here, the change of the physical properties of $La_{2-x}Sr_xCuO_{4-y}$ is described.

Oxygen deficiency has various effects on the Cu-based oxides. Generally, there are two effects. First, it generates defects in the lattice which causes a suppression of the superconductivity. The second problem is that oxygen deficiency causes electron doping, which traps holes in the CuO_2 plane, which in turn influences the superconductivity. When we think about cuprate superconductivity, the possibility of the existence of oxygen deficiency should be taken into account.

The effects with oxygen deficiency have been widely investigated. They can be summarized as follows. At first, it induces the structural change (Fig. 4.7 (a)). Given a constant Sr amount, as oxygen deficiency Δy increases, a-axis extends whereas c-axis shrinks, resulting in an increase of the cell volume. Secondly, the maximum amount of

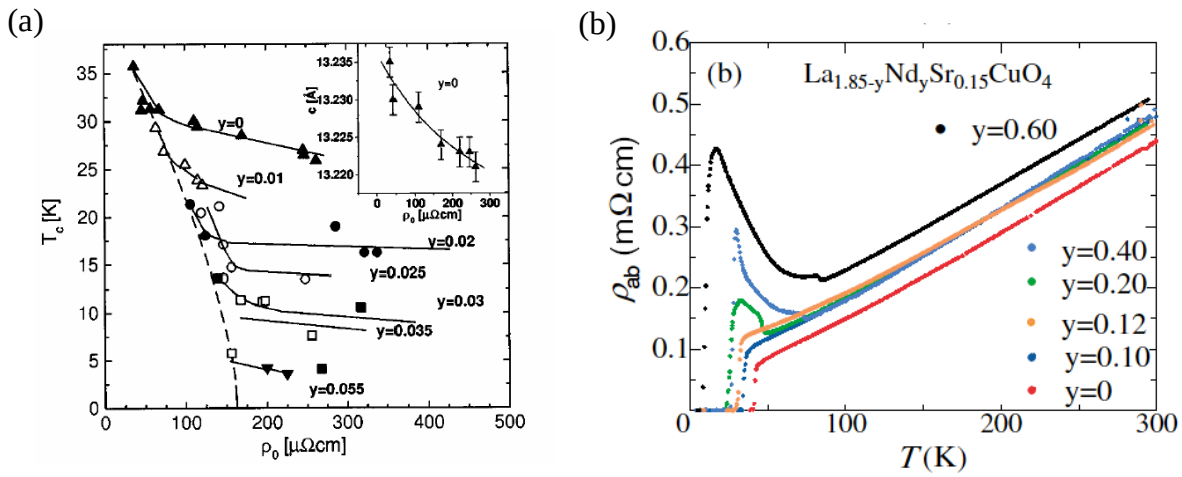

Figure 4.8: (a) T_c as a function of residual resistivity for $La_{1.85}Sr_{0.15}Cu_{1-y}Zn_yO_4$ [39]. All lines are guide for the eye. The dashed line is drawn through the points for the least resistive samples. The solid lines connect the data for different values of y. Inset shows c-axis lattice parameters as a function of the residual resistivity for the films without Zn. (b) Temperature dependence of the in-plane resistivity for optimally doped $La_{1.85-y}Nd_ySr_{0.15}Cu_{1-y}O_4$ in which disorder is introduced by changing the content of Nd [40]. For increasing Nd content, T_c monotonically decreases.

oxygen deficiency depends on Sr content (Fig. 4.7 (b)). This might be due to changes in the lattice spacing induced by the substitution of different sized ion. Next, T_c becomes more sensitive as oxygen deficiency increases (Fig. 4.7 (c)). The rate of the decrease also depends on the Sr content. To sum up, we can depict the phase diagram of T_c with different oxygen deficiency (Fig. 4.7 (d)).

4.3.4 Impurity doping

Superconducting properties are strongly suppressed by disorder induced by impurities. There are many reports confirming the effects of impurities. Other than oxygen deficiency, impurities can be categorized into two types: impurities on the CuO_2 planes and those out side of the CuO_2 planes.

In both cases, the effects of impurities appear in the correlation between T_c and resistivity. With increasing amount of impurities, the T_c decreases and resistivity increases, even though doped carrier concentration is the same. When the resistivity exceeds a threshold, T_c eventually disappears. This relationship can be scaled as shown in Fig. 4.8 (a). We can see some dispersion in the samples with the same amount of impurities. This implies that parameters other than resistivity affect the T_c behavior, for example, c-axis length and oxygen vacancy [39]. As shown in Fig. 4.8 (b), the change of resistivity is basically the same when doping impurities in the reservoir layer. According to Ref. [40], the upturn at low temperatures observed for $y \geq 0.12$ is due to the development of stripe order.

Chapter 5

Steps in the growth optimization

5.1 Introduction

In this Chapter, the optimization of the laser conditions during the growth of $La_{1.85}Sr_{0.15}CuO_4$ thin films will be discussed. First, we changed the spot size while keeping the laser energy constant. We found the relationship between the morphology, crystallinity, and resistivity. Based on this investigation, we next considered the cooling procedure. As a result, we successfully determined the optimal cooling procedure required to have a long *c*-axis and high-quality superconductivity. Under this procedure, we fabricated samples with various laser densities at the constant spot sizes. We successfully concluded that low laser density, using a wide spot size, is appropriate to make high-quality thin films. The difference between the optimal growth condition which we found, and those previously reported will be discussed. The possible mechanism which can explain why low laser density realizes high-quality films in our study will also be proposed.

5.2 Experimental

All films were grown on $LaSrAlO_4$ (001) substrates using a $La_{1.85}Sr_{0.15}CuO_4$ target at a temperature of 780 °C and oxygen partial pressure of 1.0×10^{-2} Torr, which had been optimized in advance. The laser conditions and the cooling procedures were varied. The incident angle of the laser on the target was 45° and the target-substrate distance was fixed at 50 mm. The surface morphology was measured by AFM, and the *c*-axis length and FWHM of the film (004) peak were characterized by 2θ-ω scans using XRD. RSM was also carried out by XRD. The film thickness was *ex-situ* confirmed with a stylus profilometer. For four-probe resistivity measurements, gold contacts were attached to the film which was cut into a size of 1.0×5.0 mm^2.

We fabricated three series of samples. We first fabricated four 1000 Å $La_{1.85}Sr_{0.15}CuO_4$ films with different spot sizes of area 3.5, 5.0, 8.0, and 12.0 mm^2. The laser energy was set constant at 30 mJ. In this investigation, we cooled down after the deposition at a rate of -15 ℃/min. with the same oxygen pressure as the deposition. Second, in order to improve

Table 5.1: Summary of the cooling procedures used in the second investigation. P_a and T_a are the oxygen pressure during the cooling and the temperature during the *in-situ* post-annealing, respectively. The duration of the *in-situ* post-annealing was 30 min. For Code A and B, *in-situ* post-annealing was not carried out.

Code	cooling rate R_a (°C/min.)	P_a (Torr)	T_a (°C)
A	-15	10^{-2}	-
B	-15	10^{-2}	-
C	-10	10^{-2}	500
D	-10	10^{-1}	500
E	-10	10^{-1}	400
F	-10	10^{-1}	300

the quality of the samples, we reexamined the cooling procedure by lowering the rate to -10 °C/min., and used an *in-situ* post-annealing step. In Table 5.1, the sequences of the cooling procedures are summarized. The thickness was 1000 Å and the laser density was 0.375 J/cm^2 (8 mm^2 spot). Finally, we fabricated $La_{1.85}Sr_{0.15}CuO_4$ films with different laser fluences using spot sizes of area 2.5, 8.0, and 12.0 mm^2 with the cooling procedure of Code E (see Table 5.1), which was determined to be optimal. In this investigation, we also fabricated the samples for inductively coupled plasma (ICP) measurement in order to clarify the cation ratio of the ablated species. We fabricated these films on B-doped Si substrates at room temperature. The oxygen pressure and the laser density were 10^{-2} Torr and 0.3 J/cm^2 (12 mm^2 spot). The thicknesses of the samples for ICP measurement were ≥ 1 μm. The ICP measurement was carried out by Hitachi Kyowa Engineering Co., Ltd. Below we discuss each series of samples in turn.

5.3 Spot-size variation

Comparing four samples which were fabricated using the spot sizes of area 3.5, 5.0, 8.0, and 12.0 mm^2 (total laser energy = 30 mJ), we found a clear correlation between the morphology, crystallinity, and resistivity. As shown in Figs. 5.1 (a1) - (a4), there are two types of surface. One type is covered with rectangular precipitates on top of a screwed terrace, as observed in Figs. 5.1 (a1), (a3), and (a4). The other is a surface with many circular islands, as seen in Fig. 5.1 (a2). In comparison with the XRD analysis shown in Fig. 5.1 (b), we can recognize a trade-off in these samples. The former have shorter *c*-axis and higher crystallinity, while the latter have longer *c*-axis and lower crystallinity. From this trend, we see that higher crystallinity is achieved at the cost of forming precipitates, and the origin of the longer *c*-axis without precipitates is due to some repulsive disorder inside the film. As expected, the trend of the resistivity with spot area, as shown in Fig. 5.2 (a), follows the changes of the surface morphology and the crystallinity. The first three samples show a sharp superconducting transition, whereas the final sample has a large resistivity, an upturn just before the onset of superconductivity, and a broad

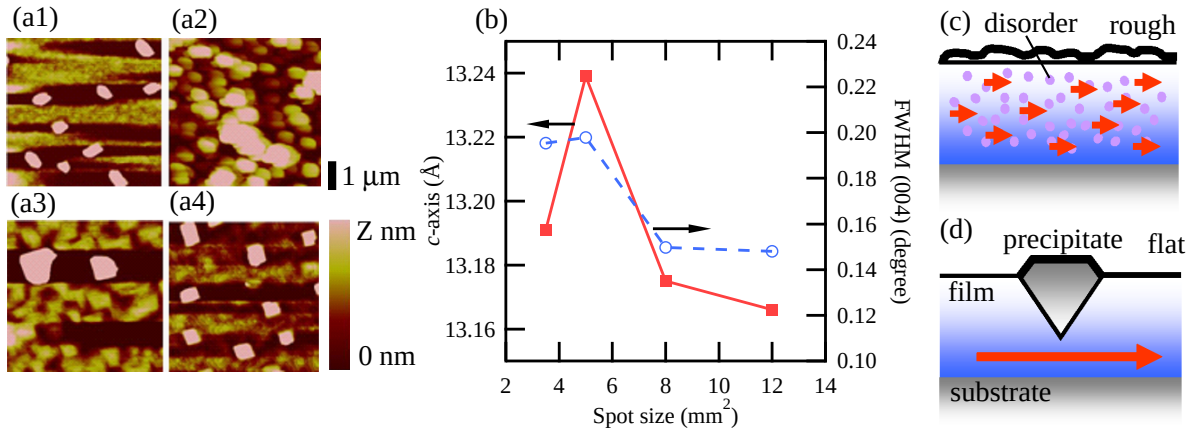

Figure 5.1: (a) The surface morphology of the films with thickness 1000 Å, measured by AFM. The laser spot sizes and the vertical scales Z are (a1) 3.5 mm^2 and Z = 5.0, (a2) 5.0 mm^2 and Z = 5.0, (a3) 8.0 mm^2 and and Z = 30, and (a4) 12.0 mm^2 and Z = 5.0. (b) c-axis length and FWHM of the (004) peak plotted as a function of the spot size. The solid lines indicate the c-axis, and the dashed lines the FWHM of the film (004) peak fitted in the 2θ-ω scan. Schematic images of (c) films containing large disorder and (d) films with precipitates.

transition.

The fact that Cooper pairs are easily broken by impurities and grain boundaries in the CuO_2 planes supports this correlation between the surface morphology, crystallinity, and superconducting behavior. As shown in Fig. 5.1 (c), when the surface is rough and the film contains much disorder, the in-plane conducting path is expected to be significantly affected. In fact, the sample made with the spot size of area 5 mm^2 has a low T_c and shows a relatively high resistivity throughout the measured temperature range as shown in Fig. 5.2 (a). In addition, there are many reports which observed a resistivity upturn. According to these reports, the possible origins are disorder and localization of the carriers caused by the impurity potentials or point defects [8, 33, 34]. On the other hand, the situation where the precipitates appear on the surface and the crystallinity is enhanced can be illustrated as shown in Fig. 5.1 (d). When precipitates grow, the excess chemical components accumulate to the precipitates and move the film closer to stoichiometry. J. P. Gong *et al.* previously suggested a similar correlation observed in $YBa_2Cu_3O_{7-\delta}$ thin films [43]. The growth of precipitates is one of the ways to achieve high-quality transport properties in superconducting film.

However, the quality of our films is still far from that of previously reported ones. We consider Fig. 5.2 (b) from the view point of the relationship between T_c and the resistivity at room temperature. In general, as the Sr dopant concentration increases, T_c reaches a maximum at the optimal doping regime, whereas the resistivity monotonically decreases, resulting in a dome-like curve as indicated by the previous literature data shown in Fig. 5.2 (b). As for the properties of our films, even though the relationship between T_c and

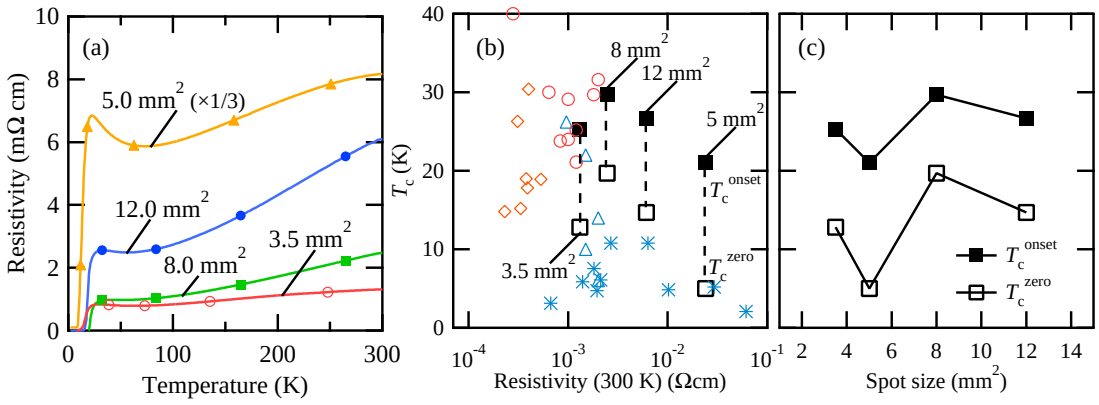

Figure 5.2: (a) Resistivity as a function of temperature for samples grown with spot sizes of 3.5, 5.0, 8.0, and 12.0 mm^2, respectively. The vertical scale for the 5.0 mm^2 sample is reduced by a factor of three for clarity. (b) and (c) show T_c as a function of resistivity at room temperature for various spot sizes. For reference, literature data shown in (b), taken from Refs. [19, 23, 41, 42]. Open diamonds, open circles, and open triangles indicate T_cs of the overdoped, optimally doped, and underdoped $La_{2-x}Sr_xCuO_4$ thin films grown on $LaSrAlO_4$ (001) substrates. Asterisks indicate T_cs of the underdoped samples which have an upturn in the resistivity, as seen in the 5.0 mm^2 spot size sample.

resistivity shows a similar dome-like curve, the absolute values of resistivity are higher by one order of magnitude. This reflects that there still remain disorder in our films, even in those with precipitates, which brings about the high resistivity. As another possibility, the concept of the effective thickness may help to understand this high resistivity. When the films have large precipitates which are buried deep into the film as shown in Fig. 5.1 (d), the effective thickness of the film in which current passes becomes smaller than the thickness measured by the profilometer. If this is the case, the resistivity ρ, which is calculated using $\rho = Rwt/l$ (here R is the resistance, w the width, t the thickness, and $l$the length) is smaller than the values plotted in Fig. 5.2 (b), which is calculated using the thicknesses measured by the profilometer. It is, however, unlikely that the effective thickness is one order of magnitude smaller than the thickness measured by the profilometer. Thus, the high resistivity in our films is probably due to disorder inside the films. Precipitates accumulate the excess chemical components to some extent, but cannot kill disorder completely.

As shown in Fig. 5.2 (c), we cannot see a clear correlation between the spot sizes and T_c, even though there have been several reports about the relationship between the spot size and the cation ratio which is one of the crucial parameters to determine the physical properties in transition metal oxides [13, 14]. This is because of the existence of precipitates. As discussed the above, they exclude excess atoms and enhance the crystallinity of the region where the conducting carriers travel so that we cannot conclude that Fig. 5.2 (c) reflects the element composition which is supplied from the target to the substrate. In order to clarify the relationship between the spot sizes and T_c, further optimization is

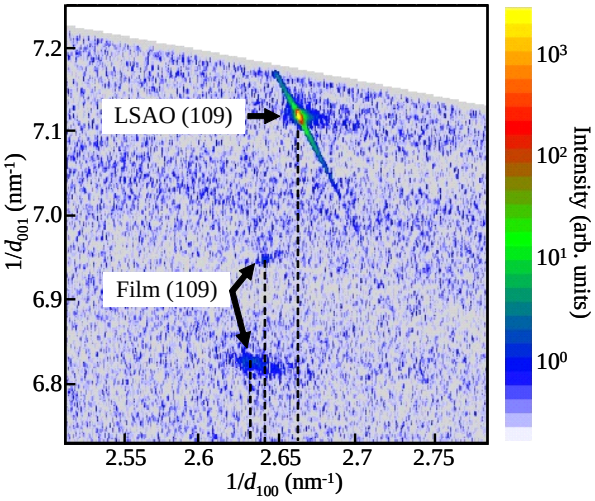

Figure 5.3: RSM around the film peak (109) of the sample with the spot size of area 8 mm^2 measured by XRD.

required to find the growth condition which can eliminate the precipitates and achieve a flat surface with high crystalinity simultaneously. Then, the element composition in the final film which is detected from resistivity and XRD measurements would be consistent with that which is supplied from the target to the substrate. This means not only to find the optimal laser condition for the stoichiometric deposition, but also to understand the mechanism of generating the precipitates.

In addition, what makes the film quality worse is the film relaxation. In Fig. 5.3, we can see the two separated peaks originating from film (109). The weaker peak indicates the relatively strained part without the precipitates, and the stronger peak represents the relaxed part due to the precipitates as illustrated in Fig. 5.1 (c). In general, the film relaxation occurs as a result of off-stoichiometry in the film and the existence of precipitates. Compared to the bulk values of $c = 13.23$ Å and $a = 3.777$ Å, the out-of-plane c-axis length (13.18 Å) shrinks, and the in-plane a-axis length (3.795 Å) expands (the values were calculated from the stronger film (109) peak). As discussed in § 4.3.1, this relaxation leads to a decrease in T_c.

In conclusion, high-quality films were obtained at the cost of precipitates. In order to obtain superconducting films showing high-quality transport properties, precipitates should be generated. There still remains the question of off-stoichiometry and disorder. We need to eventually eliminate the precipitates and achieve flat surface and highly crystalline films. On the basis of these results, we should reconsider the generation process of the precipitates and reexamine the laser conditions, which strongly affects the film stoichiometry.

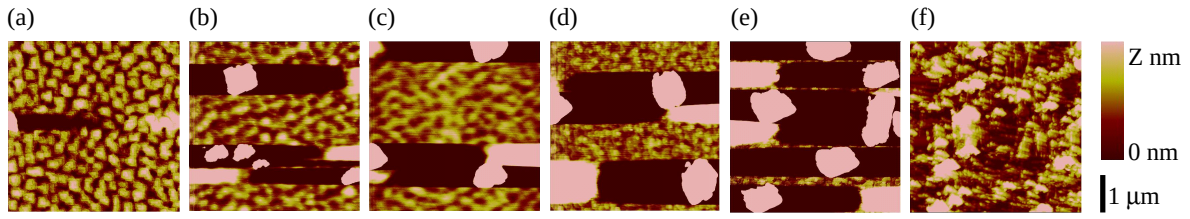

Figure 5.4: AFM images of the samples cooled in the procedure Code (a) A, (b) B, (c) C, (d) D, (e) E, and (f) F. The vertical scales are (a) Z = 3, (b) Z = 2, (c) Z = 2, (d) Z = 2, (e) Z = 2, and (f) Z = 30.

5.4 Improvement of the cooling procedure

The generation mechanism of the precipitates on the surface of thin films depends on a wide variety of factors. As well as the growth conditions such as temperature, oxygen pressure, and laser conditions, small differences of the film thickness and rate of temperature change also affect the growth process. For this set of experiments we changed only the cooling procedure. Films were fabricated as explained in § 5.2, and cooled down following the procedure in Table 5.1. Thickness was set constant at 1000 Å. We used a laser density of 0.375 J/cm^2 (8 mm^2 spot). Changing from Code A to F, the cooling rate R_a is reduced and the oxygen pressure during cooling, P_a, was increased. Thus we can regard the trend from A to F as growing the precipitates progressively more slowly.

As shown in Fig. 5.4, the volume of the precipitates increases from Code A to E but then decreases again for F. This is consistent with the expectation that the slower cooling rate and *in-situ* post-annealing are suitable for the growth of the precipitates. These samples all have relatively flat surfaces with larger rectangular precipitates. The reason why Code F has quite a rough surface is possibly due to the fact that we cannot stabilize the PID control at low temperatures (below 350 °C).

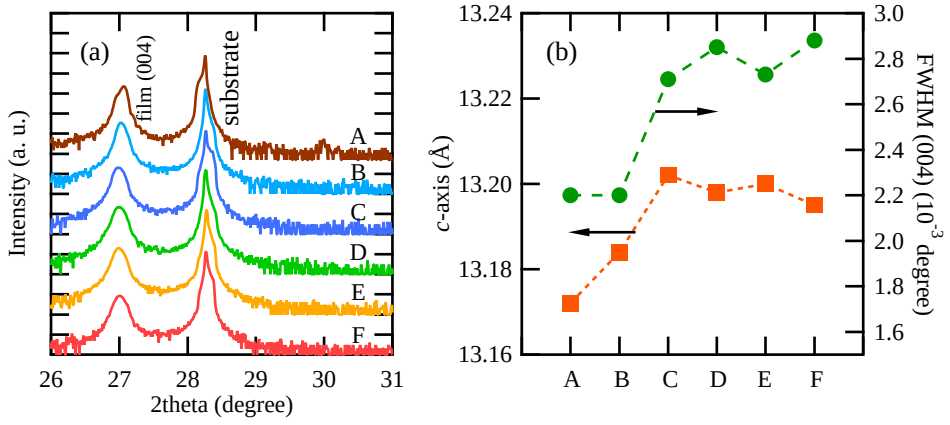

Figure 5.5: (a) 2θ-ω scans of samples annealed using procedures of Code A - F. (b) c-axis length and FWHM of the (004) peak calculated from 2θ-ω scans.

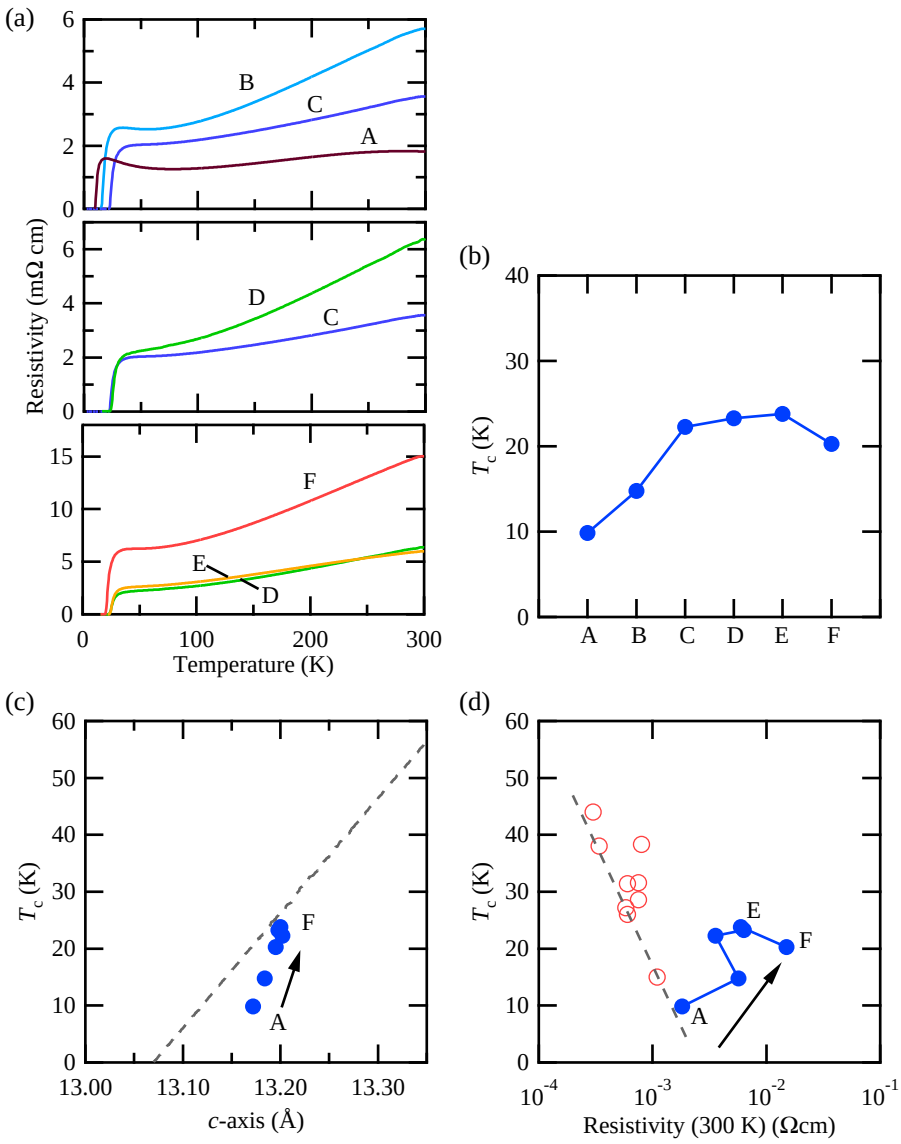

Figure 5.6: (a) Resistivity as a function of temperature. (b) T_c for samples cooled down using the procedures Code A - F. (c) T_c as a function of c-axis length. The dashed line is from Ref. [41]. (d) T_c as a function of resistivity at room temperature. Opened circles are selected from Refs. [19, 23, 41, 42]. The dashed line is a guide to the eye.

All films are epitaxially grown as we can see from Fig. 5.5 (a). The value of FWHM is increased by three orders of magnitudes as shown in Fig. 5.5 (b) compared with Fig. 5.1 (b) (in both cases, the thicknesses were set at 1000 Å). Even though the values of the FWHM slightly increase, the variation is small compared with the *c*-axis lattice constant variation. What should be noted is that the *c*-axis length expands from Code A to F. In the previous investigation, a decrease of the *c*-axis was one of the issues. Thus this effect can be addressed to some extent by *in-situ* post-annealing. However, considering that the bulk *c*-axis length is 13.23 Å, there remains room for improvement. One of the limiting factors we believe is the existence of precipitates.

The behavior of resistivity is summarized in Fig. 5.6 (a). Here we can recognize that the superconducting properties are enhanced from Code A to E. As plotted in Fig. 5.6 (b), T_c monotonically increases. In addition, as shown in Fig. 5.6 (c), T_c can be scaled with the *c*-axis length. This trend corresponds to the general trend between T_c and *c*-axis length as explained in § 4.3.1. Thus, it is likely that the slow and steady cooling treatment makes the *c*-axis longer, resulting in enhanced superconducting properties. However, the relationship between the T_c and resistivity differs from the general trend. As shown in Fig. 5.6 (d), the T_c of our samples increases as the resistivity increases, whereas T_c increases as the resistivity decreases. This anti-correlation is probably due to the existence of precipitates. As suggested previously, precipitates disturb the conducting carriers so that they can be the origin of high resistivity. Going from Code A to E, the volume of the precipitates monotonically increases. This fact can explain the relationship shown in Fig. 5.6 (d).

The relationship between the T_c and resistivity has been observed in impurity doping investigations [39, 44]. According to these works, the dispersion seen in Fig. 5.6 (d), which is conected by the solid lines, originates from the presence oxygen vacancies, not from the impurities in the CuO_2 planes [39], suggesting that, in our films, oxygen is possibly not supplied sufficiently. Or, the presence of the precipitates may result in the mechanism for oxygen to easily defect from the film, or to be taken in the precipitates.

From these results and discussions, we confirmed that the cooling procedure of Code E is the best in terms of superconducting properties. The clear correlation between T_c and *c*-axis was observed, implying that the quality of the films was improved closer to that of the previous reports. Using this cooling procedure, we next re-optimize the laser conditions more precisely.

5.5 Optimization of the laser conditions

In order to reconfirm the laser conditions, we fabricated $La_{1.85}Sr_{0.15}CuO_4$ films by changing the laser fluence using spot sizes of area 2.5, 8.0 and 12.0 mm^2. In this series of samples, we used the cooling procedure of Code E. The thickness of the films was 1000 Å for the 2.5 and 8.0 mm^2 spot area samples, and 4000 Å for the 12.0 mm^2 spot size sample.

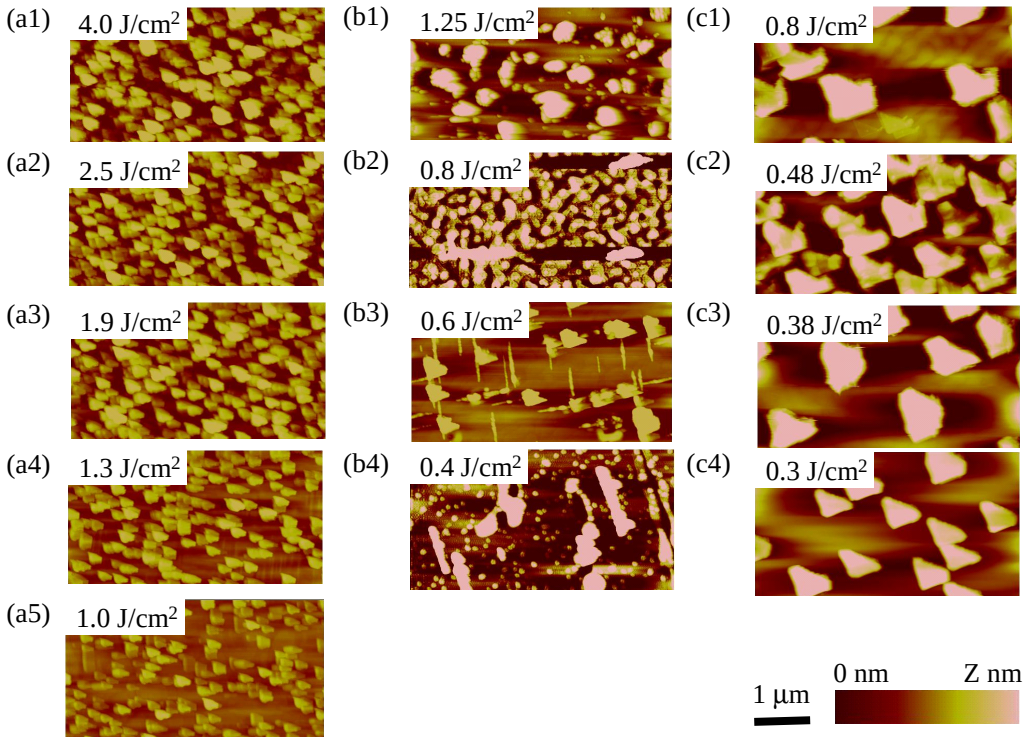

Figure 5.7: AFM images. The spot sizes are (a) 2.5, (b) 8.0, and (c) 12.0 mm^2. The vertical scales Z = (a1) 30, (a2) 30, (a3) 30, (a4) 30, (a5) 30, (b1) 50, (b2) 2, (b3) 20, (b4) 10, (c1) 30, (c2) 100, (c3) 100, and (c4) 10.

First the AFM measurements are displayed in Fig. 5.7. Comparing these results and the previous two investigations shown in Fig. 5.1 (a) and Fig. 5.4, there is no common feature except for the spot area of 12.0 mm^2. Limiting the discussion to the series of 12.0 mm^2, we can see similar precipitates on the surfaces, even though the shapes are slightly different. The difference may come from the difference of the thickness. In contrast, different characteristics appear in the series of 2.5 and 8.0 mm^2. While the surfaces are covered by circular islands in the series of 2.5 mm^2, there is no trend in the series of 8.0 mm^2. We cannot see a strong relationship between the morphology and the laser conditions from these results.

Next, let us consider the relationship between the resistivity and the laser conditions. As shown in Fig. 5.8 (a), there is an obvious correlation. In all the series of samples, the films are insulating at high laser fluence, but superconducting at low laser fluence. The resistivity results resemble the systematic trend of Sr doping concentration: gradually changing from the underdoped regime to the optimally doped regime as the laser fluence decreases [8]. This trend can be understood based on the picture of the composition variation in the plume. From the well studied PLD growth of $YBa_2Cu_3O_{7-\delta}$ films [45, 46], heavy atoms expand wider than light ones as illustrated in Fig. 5.8 (c). In our case, La (atomic weight: 138.9) is heavier than Sr (87.6) and Cu (63.5). Both plumes of the heavy and light atoms in the plume expand as the laser density increases. If we compare the ratio ρ defined by (num. of heavy atoms) / (num. of light atoms) as a function of the

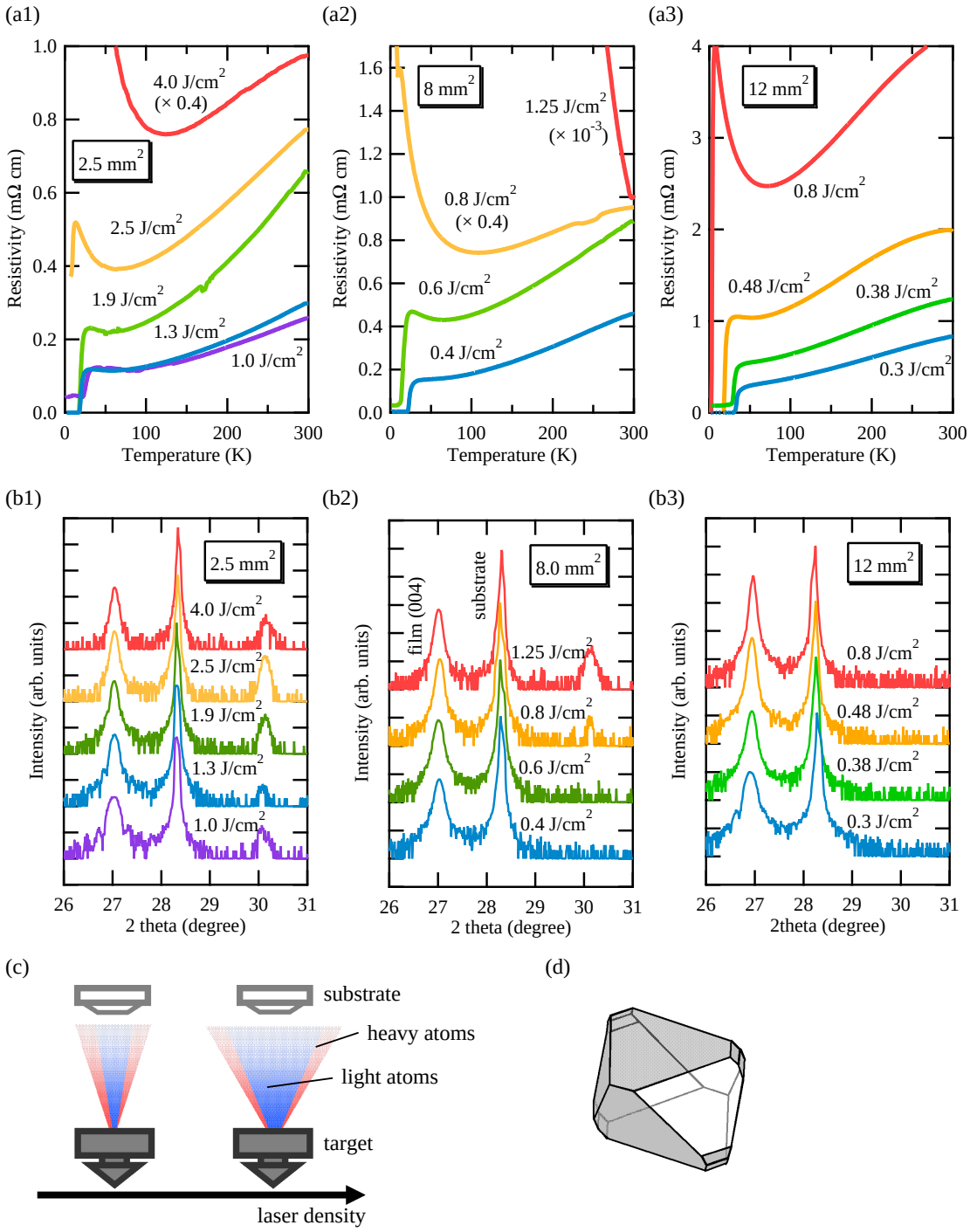

Figure 5.8: (a) Resistivity of $La_{2-x}Sr_xCuO_4$ thin films as a function of temperature. All films were grown on $LaSrAlO_4$ (001) substrates using the $La_{1.85}Sr_{0.15}CuO_4$ target. The vertical scale for the (a1) 4.0, (a2) 1.25 and 0.8 J/cm^2 samples are reduced by a factor of 0.4, 10^{-3} and 0.4, respectively for clarity. (b) 2θ-ω scans around the film (004) peak. The satellite peaks present in (b1) and the 1.25 and 0.8 J/cm^2 samples in (b2) are the impurity peaks of α-La_2O_3 (011). (c) Schematic pictures of the plume distribution for different laser density. Heavy atoms expand wider than light ones. As the laser density increases, the angular distribution becomes wider. The relative amount of the light atoms to the heavy ones at the substrate becomes larger for the low laser density than for the high laser density. (d) Monoclinic crystal structure of CuO.

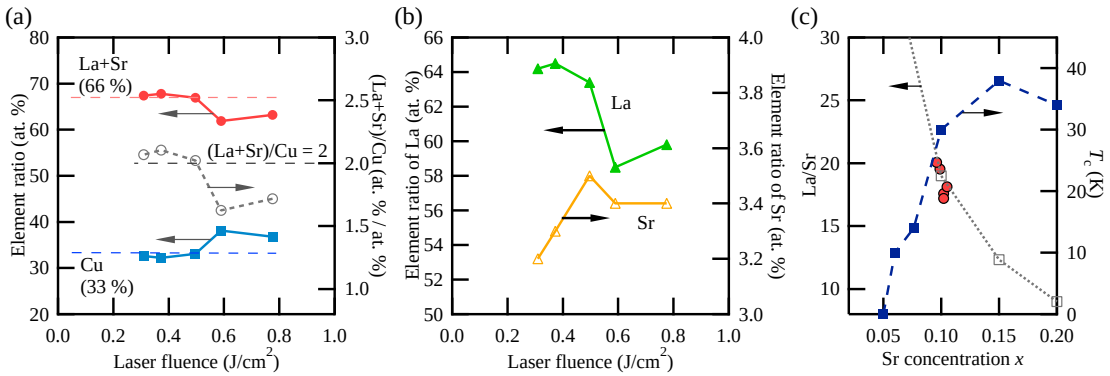

Figure 5.9: (a) Element ratio of (La+Sr) and Cu plotted as a function of the laser density. The value of (La+Sr)/Cu is also shown. (b) Element ratio of La and Sr as a fuction of the laser density. Both (a) and (b) are measured by ICP. (c) The value of La/Sr and T_c are plotted as a function of Sr concentration x in the fomula $La_{2-x}Sr_xCuO_4$. Closed circles are the values of La/Sr calculated from the values of (b). Open squares connected by dotted line represents the nominal values of $(2-x)/x$. Closed squares connected by dashed line shows T_c as a function of Sr concentration from Ref. [8].

laser density for the case of high laser density and low laser density, we can obtain [13, 14]

$$\rho(\text{low laser density}) \leq \rho(\text{high laser density}). \tag{5.1}$$

Following this scenario, we can speculate that the amount of La decreases while Sr and Cu increase as the laser density decreases. The resistivity behavior supports this speculation as can be seen in Fig. 5.8 (a). Combining these results with the AFM pictures shown in Fig. 5.7, the morphologies of Fig. 5.7 (a) and (c) may result from a lanthanum rich compound and a strontium and a copper rich compound, respectively.

In XRD results, as shown in Fig. 5.8 (b), we can see the similar trend to be consistent with the scenario which is predicted from the resistivity trend. The impurity peaks appear at around $2\theta = 30°$ of the samples with high laser fluence, which may originate from the α-La_2O_3 (011) peak, $2\theta = 30.018°$. The intensity of the impurity peak decreases as the laser fluence decreases, disappearing below 0.6 J/cm^2. The presence of a clear peak suggests that the relative volume of the impurity is significant and expected to be distributed throughout the film. However, as long as the resistivity properties of the 1.9 J/cm^2 (2.5 mm^2 spot), 1.3 J/cm^2 (2.5 mm^2 spot), 1.0 J/cm^2 (2.5 mm^2 spot) samples are concerned, the impurities do not act as scatters to the conducting carriers. From this point, the phases of $La_{2-x}Sr_xCuO_4$ and the impurities are expected to be separated inside the film. When the laser fluence is low and the spot size is large, excess Sr and Cu are possible candidates to form precipitates according to the angular distribution of the species in the plume. Furthermore as shown in Fig. 5.8 (d), the shape of the precipitates in the AFM pictures of Fig. 5.7 (c) is similar to that of CuO.

In order to confirm the element ratio of the films, we carried out ICP measurements. As noted in § 5.2, we fabricated samples under the conditions of the oxygen pressure of

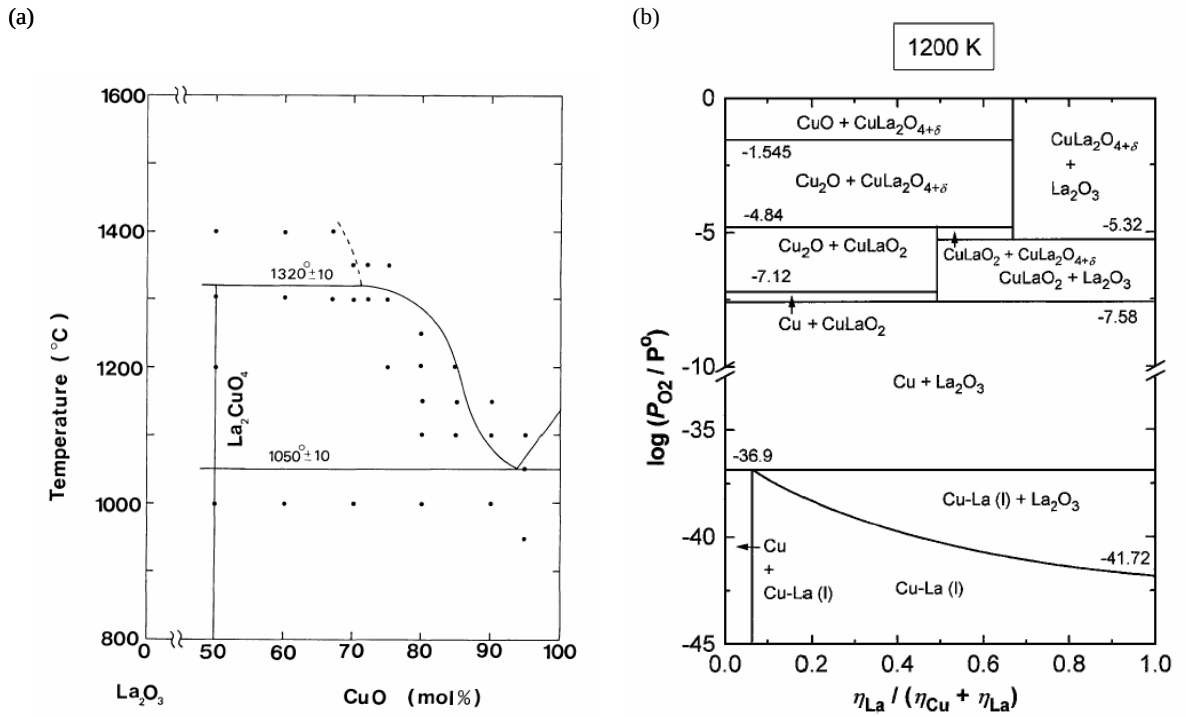

Figure 5.10: (a) Phase diagram of the system La_2O_3-CuO in air [47]. (b) Oxygen chemical potential diagram for the system Cu-La-O at 1200 K [48].

10^{-2} Torr and the laser condition of 0.3 J/cm^2 (12.0 mm^2 spot). In Fig. 5.9, the data of ICP measurements are summarized. When the laser density is lower than 0.5 J/cm^2, the composition gets closer to stoichiometric as shown in Fig. 5.9 (a). Thus, we can understand why the superconducting properties were enhanced as the laser density decreased as shown in Fig. 5.8 (a), and we can conclude that the low laser density is suitable to transfer $La_{2-x}Sr_xCuO_4$ from the target to the substrate maintaining stoichiometry. However, when the laser density is higher than 0.6 J/cm^2, the opposite trend to our expectation occurred. Even though we speculated that the amount of La increases and those of Sr and Cu decrease as the laser density increases, according to ICP results, the La component decreases and that of Sr and Cu increase, as shown in Figs. 5.9 (a) and (b).

As one possible explanation, we can consider incongruent melting deposition, which occurs when the laser density provides insufficient energy, near the laser ablation threshold. In this type of deposition, the cation ratio ρ defined in Eq. 5.1 follows [49],

$$\rho(\text{low laser density}) \;\geq\; \rho(\text{high laser density}). \tag{5.2}$$

Actually, a similar phenomenon has been reported in $YBa_2Cu_3O_{7-\delta}$ thin films [50]. Due to incongruent melting deposition, it is possible that this effect dominates the observed trend. It is, however, unlikely that this is the case, because this cannot explain the XRD results. According to Fig. 5.8 (b), the impurity peak appears when the laser density is high and seems to originate from La_2O_3. It is unlikely that La_2O_3 is formed when there

is a La deficiency. As shown in Fig. 5.10 (a), the phase of La_2CuO_4 is stable with excess Cu [47]. In addition, according to the oxygen potential diagram as shown in Fig. 5.10 (b), the components of CuO and La_2O_3 are expected to stabilize with the cation ratios under high fluence and low fluence, respectively, even though we speculated the opposite from the resistivity and XRD results (Fig. 5.8).

The re-evaporation of the cation is one of the ways to explain this behavior. Because the deposition process is carried out at a temperature of 780 °C, the cations can be vaporized by heat, disappearing from the substrate. On the other hand, this effect can be neglected in the fabrication process for the ICP samples, because it is carried out at room temperature. Based on this scenario, a large amount of the Cu atoms must have disappeared due to the high temperature during growth. Cu is known to be volatile, and excess Cu was added to the target to compensate the possible re-evaporation of Cu in some cases [19]. However, it is unlikely that the amount of cations changes from the situation in Fig. 5.9 (a) to that in Fig. 5.8 (a3).

This contradiction possibly indicates that the element composition in the final film which is detected from resistivity and XRD measurements is different from that which is supplied from the target to the substrate. Even though ICP can detect *all of the elements on the substrate*, it is not always true that all of them contribute to the properties of resistivity and XRD. Considering the fact that all films have precipitates on their surfaces, the crystallization process of crystalline film and the generation process of precipitates can be concluded to be a key issue to understand these results.

Finally, we confirmed the Sr concentration in the films calculated from the ICP measurement. As shown in Fig. 5.9 (c), our films stay in the underdoped region. Considering Figs. 5.9 (b) and (c), it is suspected that the amount of Sr in the target is less than our expectation.

5.6 Comparison with the previous reports

Historically, the technique of PLD developed through making $YBa_2Cu_3O_{7-\delta}$ thin films for microwave devices, for example [51]. It is quite recent that the importance of the laser condition for stoichiometric deposition in PLD has come to light [13, 14, 49]. In this sense, this study is the first investigation focusing on the optimization of the laser condition in the growth of $La_{2-x}Sr_xCuO_4$ thin films. The results shown in Fig. 5.8 and Fig. 5.9 support that our growth conditions are optimized to maintain stoichiometry.

However, there has been no report finding the same growth condition as our optimal growth condition for $La_{2-x}Sr_xCuO_4$, namely, the oxygen pressure of 10^{-2} Torr and the laser condition of 0.3 J/cm^2 (12 mm^2 spot). Many PLD grown films investigated in the past used the high oxygen pressures, exceeding 10^{-1} Torr, and a high laser density with a small spot size (for example, see Ref. [7]). As representative examples, pressures and laser densities of 130 mTorr and 1.5 J/cm^2 (no information about spot size) were reported in Ref. [35], 130 mTorr and 1.0 J/cm^2 (no information about spot size) reported

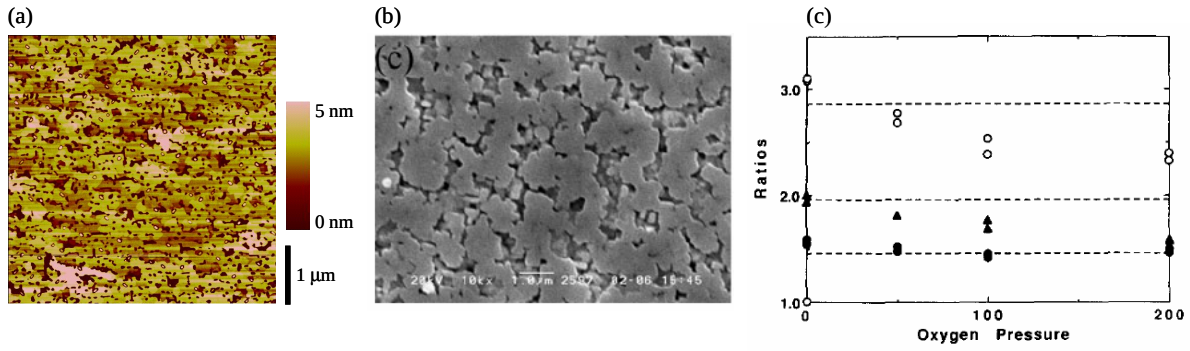

Figure 5.11: (a) AFM image of the sample fabricated under the oxygen pressure of 100 mTorr. The laser density was 0.375 J/cm^2 (8 mm^2 spot). (b) A scanning electron micrograph taken from Ref. [55]. (c) Ratios of elements in film versus oxygen pressure for a target-substrate distance of 6 cm with fluence = 1.1 J/cm^2, and 1.7 $\times$ 5.1 mm^2 spot size [45]. Open circles, closed triangles, and closed circles indicate Cu/Y, Ba/Y, and Cu/Ba, respectively. Dashed lines represent the target composition. (d) Phase diagram of the system La_2O_3-CuO in air [47]. (e) Oxygen chemical potential diagram for the system Cu-La-O at 1200 K [48].

in Ref. [52] and 10 mPa with O_3 (no information about laser condition) [19]. Most of the $La_{2-x}Sr_xCuO_4$ films were fabricated using sputtering [53, 54] and MBE. Many MBE studies were carried out in high pressure oxygen atmosphere or ozone atmosphere [9, 11, 17, 23, 41]. While there are only a few groups who reported the fine tuning of the laser conditions during the growth of $La_{2-x}Sr_xCuO_4$ films, $YBa_2Cu_3O_{7-\delta}$ films have been intensely studied. According to these studies, almost all of these films were grown under high oxygen pressure exceeding 10^{-1} Torr and high laser density around 1.2 J/cm^2 [43, 45, 46, 50], in a different regime compared to the conditions found in this study.

We also fabricated under the oxygen pressure of 100 mTorr, but never obtained high-quality films. Even though we varied the laser density and the spot size, films showed low T_c, typically below 10 K, with a large upturn in resistivity, or often were insulating. In addition, the morphology had different characteristics from the samples fabricated under the oxygen pressure of 10 mTorr. As shown in Fig. 5.11 (a), we can see many pores on the surface. A similar morphology was observed in $YBa_2Cu_3O_{7-\delta}$ thin films grown at high pressure of 170 mTorr, as shown in Fig. 5.11 (b) [55]. According to this report, the presence of this kind of pores is a result of the copper-deficient composition in the films. It is known that the copper-deficient composition can be obtained under the fabrication of high oxygen pressure because light cations are easily scattered by the oxygen atmosphere, as shown in Fig. 5.11 (c) [45].

Two explanations can be given for the observed difference in the growth conditions. One is the difference in the local oxygen pressure near the substrate. Pressure gauge are generally positioned at a distance from the substrate. The other is the detail of the laser energy profile on the target surface which is strongly dependent on the laser and the optics. In our system, the laser spot edges are blurred (Fig. 2.2 (b)) which can lead

to stoichiometric dispersion in the ablated species.

The remaining problem is the precipitates on the film surfaces. Even though the films fabricated under the optimized conditions have high T_c and a long c-axis, the existence of precipitates is generally a sign of off-stoichiometry. This means imperfect optimization of the laser conditions. In order to remove this ambiguity, whether the laser condition was optimized or not, we need to remove oxygen vacancies, which can be a possible way to generate precipitates even under optimized laser conditions. As explained, the oxygen pressure during growth is relatively low. Even though the atmosphere with oxygen inside the chamber is probably optimized to transfer the cations from the target to the substrate, it is possibly not optimized to supply enough oxygen to the film. If the supply of oxygen is insufficient, it is easy for cations to segregate because of the missing oxygen atoms. On the basis of this discussion, ozone is a possible candidate to solve this problem. Ozone is expected to oxidize sufficiently without changing the pressure in the chamber. It is also expected that cooling in an ozone atmosphere brings about further enhancement of the superconducting properties.

5.7 Conclusion

We fabricated $La_{2-x}Sr_xCuO_4$ thin flms by PLD with various laser conditions and the cooling procedures, and studied the correlation between the morphology, crystallinity, and superconducting behavior. As a result, high-crystallinity samples with sharp superconducting transition were obtained at the cost of precipitates on the film surfaces. Through sustematic investigation of the cooling process, we determined the optimal procedure from the view point of the superconducting properties. As for the laser conditions, we found that lower laser fluence was optimal to make $La_{2-x}Sr_xCuO_4$ thin films. In spite of the optimization of the laser conditions, precipitates still remained on the surface, which indicates imperfect film quality. In order to eliminate precipitates, further improvement is required, such as installing ozone.

Chapter 6

Growth in ozone atmosphere

6.1 Introduction

The strong oxidizing power of ozone is known to dramatically enhance the superconducting properties of cuprate thin films [9, 11, 17, 23, 41, 56]. In this Chapter, we utilized ozone during the cooling procedure and the growth. As a result, we successfully eliminated precipitates on the surface and enhanced the superconducting properties. Finally, we will discuss the possible future directions to make much higher-quality films showing T_c exceeding the bulk value and to make ultra-thin films for functional devices such as photoactive devices.

6.2 Experimental

On the basis of the previous investigation in Chapter 5, we fabricated $La_{1.85}Sr_{0.15}CuO_4$ thin films on $LaSrAlO_4$ (001) substrates using a substrate temperature of 780 °C, oxygen partial pressure of 1.0×10^{-2} Torr, and laser density of 0.3 J/cm^2 (12 mm^2 spot). The film thickness was set constant at 750 Å. After fabricating five identical samples in these conditions, we cooled them down in an ozone atmosphere. The ozone pressure was varied from $10^{-5} \sim 10^{-1}$ Torr. The cooling rate and the *in-situ* annealing conditions were the same, -10 ˚C/min. with a pause at 400 ˚C for 30 min. The selected cooling procedure is Code E (see Table 5.1).

Next, we utilized ozone also during the deposition. Four $La_{1.85}Sr_{0.15}CuO_4$ thin films were fabricated using the same conditions as above, with again the thickness fixed at 750 Å. During the deposition, we varied the ozone pressures of 10^{-6}, 10^{-4}, 10^{-2}, and 10^{-1} Torr. We cooled them down in the same procedure as above, with the ozone atmosphere of 10^{-1} Torr.

6.3 Ozone cooling

As shown in Fig. 6.1 (a), all films cooled in ozone were epitaxially grown and no impurity peak appeared in the XRD. As shown in Fig. 6.1 (b), the number of precipitates on

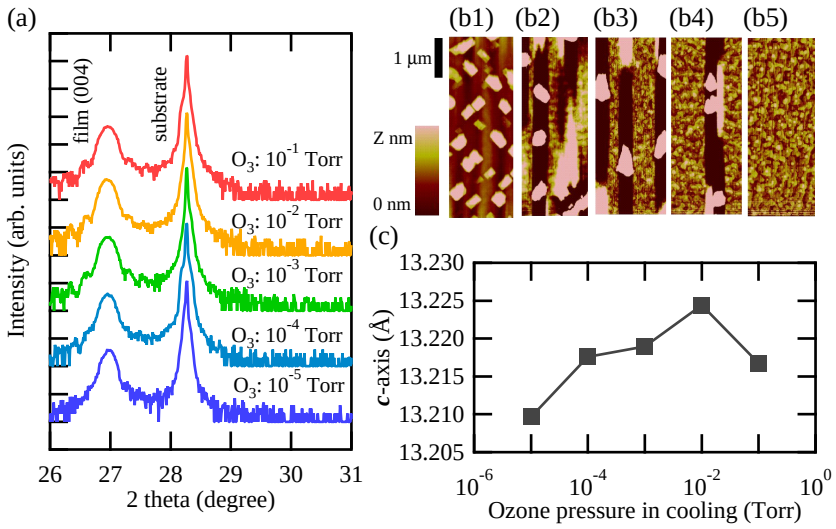

Figure 6.1: (a) 2θ-ω scans around the film (004) peak. (b) AFM pictures of the samples cooled down in the ozone pressure (in Torr) of (b1) 10^{-5}, (b2) 10^{-4}, (b3) 10^{-3}, (b4) 10^{-2}, and (b5) 10^{-1}. (c) c-axis length as a function of ozone pressure in cooling.

the surfaces gradually decreases as the ozone pressure increases. Coincidentally, c-axis expands as shown in Fig. 6.1 (c). The resistivity results are summarized in Fig. 6.2 (a). As shown in Fig. 6.2 (b), T_c monotonically increases with the ozone pressure during cooling except for the case of 10^{-1} Torr. The higher pressure ozone is obviously suitable for making high-quality superconducting films.

The trend of AFM images (Fig. 6.1 (b)) implies that the generation process of precipitates depends on the cooling step, not on the deposition step. Taking into account that the element composition deduced from the ICP measurements are stoichiometric in this laser condition as shown in Fig. 6.1 (c), the precipitates seem to be integrated inside the films, assisted by the oxidization power of the ozone. In the previous investigation of the deposition under the oxygen atmosphere, it can be concluded that the appearance of precipitates is due to the absence of oxygen after the deposition.

The correlation between T_c, c-axis, and resistivity is close to that seen in the previous reports, under the ozone cooling. As shown in Fig. 6.2 (c), T_c increases as c-axis expands. The relationship between T_c and resistivity gradually reaches to that of referencing data, as seen in Fig. 6.2 (d). Both are achieved probably due to the elimination of precipitates.

In conclusion, the previously investigated laser condition is optimal to transfer from the target to the substrate keeping stoichiometry and ozone eliminates the precipitates. Thus, we find that the growth of $La_{1.85}Sr_{0.15}CuO_4$ thin films is influenced by cooling in an atmosphere with high oxidization power.

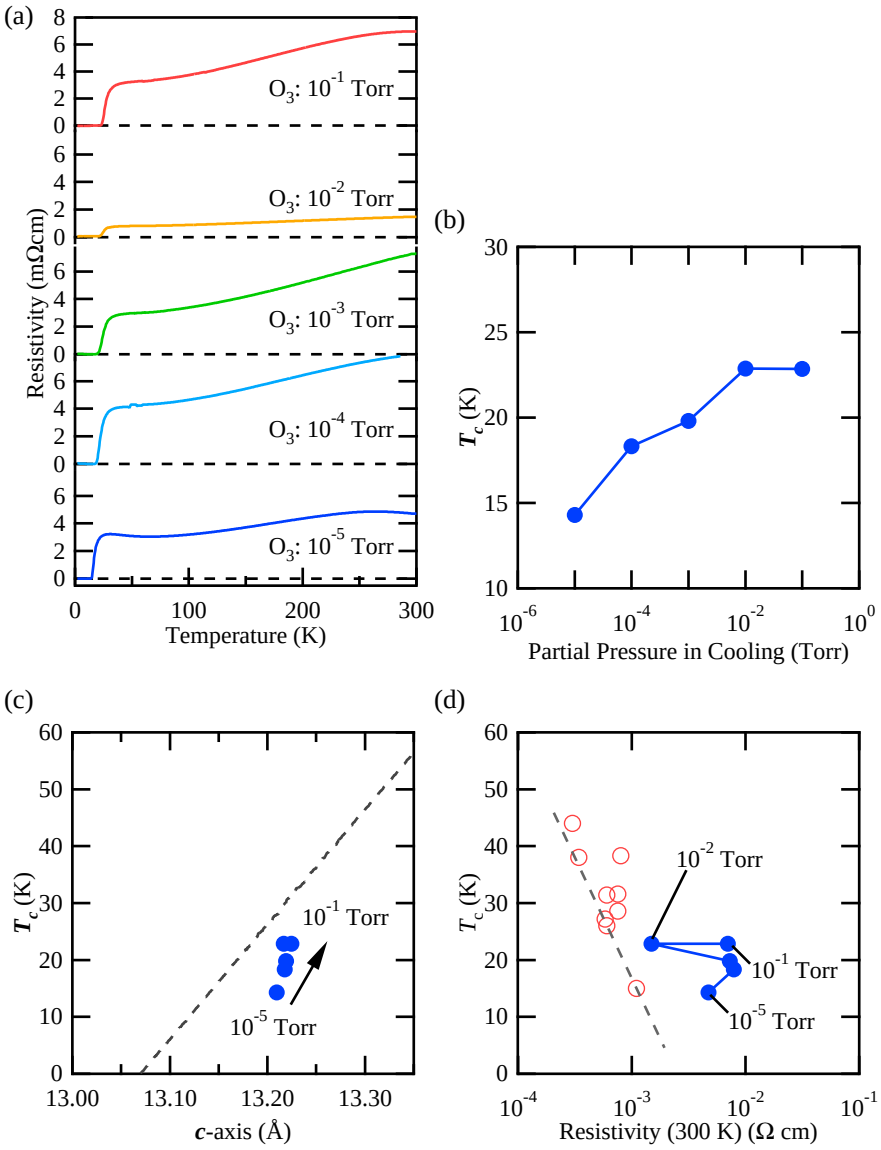

Figure 6.2: (a) Resistivity as a function of temperature. (b) T_c of the samples as a function of the cooling pressure. (c) T_c as a function of the c-axis length. The dashed line is taken from Ref. [41]. (d) T_c as a function of the resistivity at room temperature. Open circles are taken from Refs. [19, 23, 41, 42]. The dashed line is a guide for the eye.

6.4 Ozone growth

Next we deposited films with an ozone atmosphere. Samples were cooled down under the ozone atmosphere of 10^{-1} Torr. As shown in Fig. 6.3 (a), precipitates gradually disappear as the ozone pressure increases. When the pressure is 10^{-2} Torr, precipitates remain on the surface even though they disappeared when the atmosphere during growth was oxygen. This may be because the scattering processes are different between oxygen and ozone. The difference between the supply nozzles for the oxygen and ozone is another possibility. It is required to re-optimize the laser condition under ozone atmosphere. When the ozone pressure was 10^{-6} Torr, the film was amorphous.

As shown in Fig. 6.3 (b), the values of c-axis length and T_c reach a maximum at the ozone pressure of 10^{-4} Torr. Particularly, the c-axis length of 13.234 Å is close to the bulk value. However, the sample quality is not clearly enhanced since, as shown in Fig. 6.3 (c), the resistivity behavior is not sharp compared to the samples grown under an oxygen atmosphere. This also implies that a re-optimization of the growth conditions is required when we utilize ozone during deposition.

This investigation suggests that the generation process of precipitates only depends on the cooling procedure as same as the previous investigation. The atmosphere works as scatters to the ablated species during deposition, and works as oxidant to the deposited film during cooling. When the stoichiometric ablation is required, the optimizations of atmosphere and laser condition are crucial. On the other hand, when the flat and highly crystalline film is needed, the strong oxidization are necessary in order to stabilize $La_{2-x}Sr_xCuO_4$ thin films.

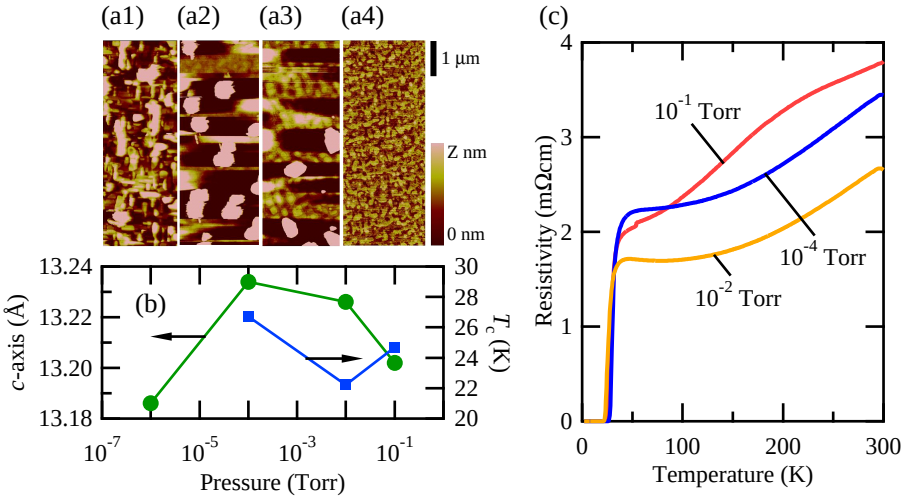

Figure 6.3: (a) AFM pictures of sample grown under ozone pressures of (a1) 10^{-6}, (a2) 10^{-4}, (a3) 10^{-2}, and (a4) 10^{-1} Torr. (b) c-axis length and T_c plotted as a function of the ozone pressure during the deposition. (c) Resistivity as a function of temperature.

6.5 Conclusion

In conclusion, we utilized ozone both during the cooling procedure and the deposition process. When we oxidized samples in the cooling process, precipitates on the surfaces gradually disappeared as the ozone pressure increased, meaning that the oxygen deficiency was successfully eliminated by ozone. This result shows that, in this case, the laser conditions were optimal to transfer the target composition to the substrate, maintaining the stoichiometry. As for the ozone utilization during growth, an enhancement of the superconducting properties was not obtained, even though c-axis length expanded. This may be due to need for a different optimization when growing in an ozone atmosphere. Further improvement is needed.

Chapter 7

Conclusion

In this study, we investigated the optimization of the growth of $La_{2-x}Sr_xCuO_4$ thin films by PLD. Part of this process required the installation of an ozone generator to the PLD system. For the enhancement of film quality and superconducting properties, necessary to proceed towards the fabrication of superlattice structures between superconducting materials and other oxides, we particularly focused on the laser conditions and the oxidization process during the deposition and the cooling procedure. As a result, we found a strong correlation between the laser density and the physical properties. In addition, the use of ozone allows us to eliminate the precipitates on the surface of the cuprate thin films using the strong oxidization power of ozone. Finally, we successfully determined the optimal growth condition of $La_{2-x}Sr_xCuO_4$ thin films: a substrate temperature of 780 °C, oxygen partial pressure of 1.0×10^{-2} Torr, and laser density of 0.3 J/cm^2 (12 mm^2 spot). Sample cooling after the deposition was performed at a rate of -10 °C/min. with an ozone pressure of 10^{-1} Torr including an *in-situ* pause at 400 °C for 30 min. We found that low laser density was suitable to obtain a stoichiometric ablation, the proposed cooling procedure was appropriate to form highly crystalline films, and the ozone utilization during cooling could suppress the precipitate generation.

These achievements are appealing for the following two reasons. Firstly, the optimal growth condition we determined is unique compared to previous reports. Our condition utilizes relatively low laser density under low pressure, while the others apply high laser density under high pressure. This difference can shed some light on the growth of oxide thin films by PLD. Secondly, we found that precipitates on the surface of the thin films can be eliminated using ozone oxidization only during the cooling procedure. This result also gives useful comprehension of the processes for deposited elements to form epitaxially crystalline films or precipitates.

On the basis of this achievement, we can make superlattice structures combining with other oxides. It is interesting to investigate various combinations and check the superconducting properties. The researches of superconductivity in superlattice are just getting started. The challenge to utilize ultra-thin films for functional devices is also promising. It can be a platform not only to approach the superconductivity in a single CuO_2 layer, to confine carriers in a small region. In order to obtain high-quality ultra-thin

films, it is known to require the precise cation-ratio control and the strong oxidization. This study paved the way for us to fabricate them.

Among the increasing attention paid to oxide heterostructures, the high-T_c superconducting superlattices and ultra-thin films have been attracting a lot of interest, because of the possibility of making functional devices and accessing the fundamental mechanism of superconductivity. This study not only provided many remarks about the growth mechanism in PLD, but also established the basis for moving in this exciting field.

Appendix A

Supplemental information of sample fabrication

When we fabricate thin films, what is emphasized is the recipe of the growth conditions such as temperature, pressure, and laser condition during deposition. In practice, it is difficult to compare the recipes from different groups. Even though we make samples referencing the recipes utilized in other systems, it is impossible to reproduce the same conditions down to the practical details. Here we describe such details focusing on the substrate preparation, the temperature monitoring, and the pressure controlling used throughout the Thesis.

i) Procedure of substrate preparation before deposition

First of all, we cut the substrates into 5 × 5 mm^2 pieces using a diamond cutter from the 10 × 10 mm^2 or 15 × 15 mm^2 sized substrates supplied by the companies.

Although the surfaces of the substrates are polished and sometimes etched by acids, there are many contaminants such as dust in air and carbon. In order to eliminate them, we have utilized acetone and methanol cleaning which is an orthodox method to clean up the surface of semiconductors. The substrate is first dipped into acetone and vibrated at the ultrasonic frequency for 5 min. after which it cleaned with methanol for 5 min. This two-step cleaning is repeated twice before loading into chamber.

The cleaned substrate is next clamped at the sample holder made with inconel. To the backside of the substrate, Pt paste is coated in order to make the contact secure and enhance the thermal conductance. Pt paste should be spread uniformly in order to avoid temperature gradient within the substrate.

Before inserting the sample holder into the main chamber, it is heated at 250 °C for 30 min. in the L/L chamber in order to bake the Pt paste. During this baking operation, the pressure of the L/L chamber is reduced at the pressure of 10^{-6} Torr.

Based on this preparation, substrates are heated in appropriate pressure following the recipe of the optimal growth condition.

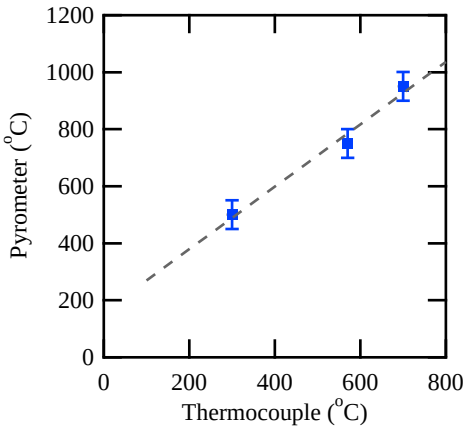

Figure A.1: The correlation between the temperature monitored by the pyrometer and the thermocouple. The value of the pyrometer has a margin of error ($\sim \pm 50$ °C) depending on the substrate and the Pt paste attaching substrate to the sample holder.

ii) Calibration of the two temperatures monitored by thermocouple and pyrometer

On the PID control installed in the PLD system, the temperature value which is monitored by the thermocouple placed near the substrate holder (Fig. 2.1 (a)) is fed back. Since the thermocouple is placed directly next to the sample, the actual temperature of the sample is likely to differ from the thermocouple readings. In order to have better accuracy for the *sample* temperature, a pyrometer focused on the sample surface is used. The calibration of the two temperature were carried out before the experiments (Fig. A.1).

iii) Pressure control in the main chamber

The relationship between the pressure of the chamber and the management procedure of each system is summarized in Table A.1. Since ion gauges can be damaged at high pressure, Baratron is used in the range above 10^{-3} Torr. When pressure goes above 10^{-3} Torr, one should first adjust the VLV output value listed in Table A.1, and then shut down the shutter. Thus, the aimed pressure is available monitored by Baratron.

Table A.1: The relationship between the pressure of the chamber and the management procedure of VLV output, shutter, and valve.

Chamber (Torr)	VLV output (Torr)	shutter (A)	valve (A)	monitoring
10^{-6}	10^{-6}	open	open	ion gauge
10^{-5}	10^{-5}	open	open	ion gauge
10^{-4}	10^{-4}	open	open	ion gauge
10^{-3}	10^{-6}	close	open	Baratron
10^{-2}	10^{-5}	close	open	Baratron
10^{-1}	10^{-5}	close	close	Baratron

References

[1] J. G. Bednorz and K. A. Müller, Z. Phys. B **64**, 189 (1986).

[2] M. Imada, A. Fujimori, and Y. Tokura, Rev. Mod. Phys. **70**, 1039 (1998).

[3] H. Kroemer, *"Quasielectric fields and band offsets: teaching electrons new tricks"*, Nobel Lecture (Dec. 8^{th}, 2000).

[4] A. Ohtomo, D. A. Muller, J. L. Grazul, and H. Y. Hwang, Nature **419**, 378 (2002).

[5] A. Ohtomo and H. Y. Hwang, Nature **427**, 423 (2004).

[6] Y. Hikita, M. Nishikawa, T. Yajima, and H. Y. Hwang, Phys. Rev. B **79**, 073101 (2009).

[7] M. Hujiben, *Interface Engineering for Oxide Electronics: Tuning electronic properties by atomically controlled growth*, Ph. D. Thesis University of Twente, Enschede, The Netherlands (2006).

[8] H. Takagi, T. Ido, S. Ishibashi, M. Uota, S. Uchida, and Y. Tokura, Phys. Rev. B **40**, 2254 (1989).

[9] A. Gozar, G. Logvenov, L. F. Kourkoutis, A. T. Bollinger, L. A. Giannuzzi, D. A. Muller, and I. Bozovic, Nature **455**, 782 (2008).

[10] G. Koster, A. Brinkman, H. Hilgenkamp, A. J. H. M. Rijnders, and D. H. A. Blank, J. Phys.: Cond. Mat. **20**, 264007 (2008).

[11] H. Sato, M. Naito, and H. Yamamoto, Physica C **280**, 178 (1997).

[12] J. Orenstein and A. J. Millis, Nature **288**, 468 (2000).

[13] T. Ohnishi, M. Lippmaa, T. Yamamoto, S. Meguro, and H. Koinuma, Appl. Phys. Lett. **87**, 241919 (2005).

[14] J. H. Song, T. Susaki, and H. Y. Hwang, Adv. Mater. **20**, 2528 (2008).

[15] S. M. Sze and K. K. Ng, *Physics of Semiconductor Devices, 2nd Ed.* (WILEY, 1981).

[16] M. Horvath, L. Bilitzky, and J. Hüttner, *Ozone* (Elsevier, Amsterdam, 1985).

[17] I. Bozovic, G. Logvenov, I. Belca, B. Narimbetov, and I. Sveklo, Phys. Rev. Lett. **89**, 107001 (2002).

[18] R. O. Suzuki, T. Ogawa, and K. Ono, J. Am. Ceram. Soc. **82**, 2033 (1999).

[19] I. Tsukada and S. Ono, Phys. Rev. B **74**, 134508 (2006).

[20] H. Yamada, M. Kawasaki, and Y. Tokura, Appl. Phys. Lett. **80**, 622 (2002).

[21] S. Kobayashi, Surf. Sci. Rep. **16**, 1 (1992).

[22] T. Shimizu and H. Okushi, Appl. Phys. Lett. **67**, 1411 (1995).

[23] H. Sato, A. Tsukada, M. Naito, and A. Matsuda, Phys. Rev. B **61**, 12447 (2000).

[24] A. Barth and W. Marx, cond-mat/0609114 (2006).

[25] A. Schilling, M. Cantoni, J. D. Guo, and H. R. Ott, Nature **363**, 56 (1993).
[26] L. Gao, J. Z. Huang, R. L. Meng, G. Lin, F. Chen, L. Beauvais, Y. Y. Xue, and C. W. Chu, Physica C **213**, 261 (1993).
[27] C. W. Chu, L. Gao, F. Chen, Z. J. Huang, R. L. Meng, and Y. Y. Xue, Nature **365**, 323 (1993).
[28] S. Uchida, Parity **23**, 4 (2008).
[29] Y. J. Uemura, L. P. Le, G. M. Luke, B. J. Sternlieb, W. D. Wu, J. H. Brewer, T. M. Riseman, C. L. Seaman, M. B. Maple, M. Ishikawa, et al., Phys. Rev. Lett. **66**, 2665 (1991).
[30] H. Zhang and H. Sato, Phys. Rev. Lett. **70**, 1697 (1993).
[31] S. Chakravarty, H. Y. Kee, and K. Völker, Nature **428**, 53 (2004).
[32] A. Iyo, Y. Tanaka, H. Kito, Y. Kodama, P. M. Shirage, D. D. Shivagan, H. Matsuhara, K. Tokiwa, and T. Watanabe, J. Phys. Soc. Jpn. **76**, 094711 (2007).
[33] R. J. Birgeneau, C. Y. Chen, D. R. Gabbe, H. P. Jenssen, M. A. Kastner, C. J. Peters, P. J. Picone, T. Thio, T. R. Thurston, and H. L. Tuller, Phys. Rev. Lett. **59**, 1329 (1987).
[34] M. Oda, Y. Hidaka, M. Suzuki, Y. Enomoto, T. Murakami, K. Yamada, and Y. Endoh, Solid State Commun. **67**, 257 (1988).
[35] M. Z. Cieplak, M. Berkowski, S. Guha, E. Cheng, A. S. Vagelos, D. J. Rabinowitz, B. Wu, and I. E. Trofimov, Appl. Phys. Lett. **65**, 3383 (1994).
[36] H. Sato, H. Yamamoto, and M. Naito, Physica C **274**, 227 (1997).
[37] A. Rüfenacht, P. Chappatte, S. Gariglio, C. Leemann, J. Fompeyrine, J. P. Locquet, and P. Martinoli, Solid-State Electronics **47**, 2167 (2003).
[38] E. Takayama-Muromachi and D. E. Rice, Physica C **177**, 195 (1991).
[39] M. Z. Cieplak, K. Karpinska, J. Domagala, E. Dynowska, M. Berkowski, A. Malinowski, S. Guha, M. Croft, and P. Lindenfeld, Appl. Phys. Lett. **73**, 2823 (1998).
[40] K. Fujita, T. Noda, K. M. Kojima, H. Eisaki, and S. Uchida, Phys. Rev. Lett. **95**, 097006 (2005).
[41] H. Sato and M. Naito, Physica C **274**, 221 (1997).
[42] M. Suzuki, Phys. Rev. B **39**, 2321 (1989).
[43] J. P. Gong, M. Kawasaki, K. Fujito, R. Tsichiya, M. Yoshimoto, and H. Koinuma, Phys. Rev. B **50**, 3280 (1994).
[44] Y. Fukuzumi, K. Mizuhashi, K. Takenaka, and S. Uchida, Phys. Rev. Lett. **76**, 684 (1996).
[45] M. C. Foote, B. B. Jones, B. D. Hunt, J. B. Barner, R. P. Vasquez, and L. J. Bajuk, Physica C **201**, 176 (1992).
[46] K. Develos-Bagarinao, H. Yamasaki, Y. Nakagawa, H. Obara, and H. Yamada, Physica C **392**, 1229 (2003).
[47] K. Oka and H. Unoki, Jpn. J. Appl. Phys. **26**, L1590 (1987).
[48] K. T. Jacob and K. P. Jayadevan, J. Mater. Sci. **37**, 1611 (2002).
[49] R. Sakai, T. Ohnishi, N. Shibata, T. Mizoguchi, Y. Ikuhara, and T. Yamamoto,

WOE14 PII-24 (2007).
[50] B. Dam, J. Rector, M. Chang, S. Kars, D. de Groot, and R. Griessen, Appl. Surf. Sci. **86**, 13 (1995).
[51] M. A. Hein, Supercon. Sci. and Tech. **10**, 867 (1997).
[52] I. E. Trofimov, L. A. Johnson, K. V. Ramanujachary, S. Guha, M. G. Harrison, M. Greenblatt, M. Z. Cieplak, and P. Lindenfeld, Appl. Phys. Lett **65**, 2481 (1994).
[53] M. Suzuki, Phys.Rev. B **39**, 2312 (1989).
[54] M. Suzuki and T. Murakami, Jpn. J. Appl. Phys. **26**, 524 (1987).
[55] K. Develos-Bagarinao, H. Yamasaki, Y. Nakagawa, and K. Endo, Supercond. Sci. Technol. **17**, 1253 (2004).
[56] W. Si, H. C. Li, and X. X. Xi, Appl. Phys. Lett. **74**, 2839 (1999).